iScience

CellPress
OPEN ACCESS

Article

A DNA-Based FLIM Reporter for Simultaneous Quantification of Lysosomal pH and Ca^{2+} during Autophagy Regulation

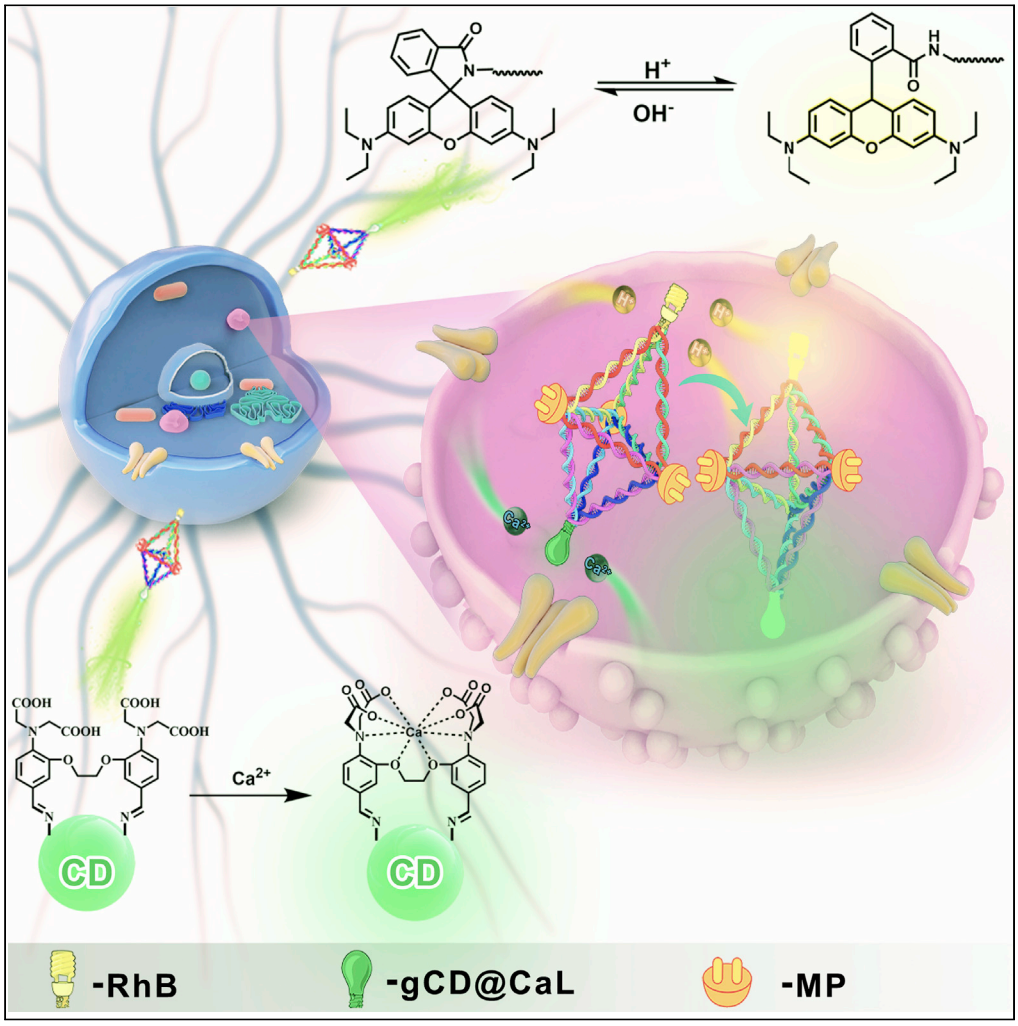

Zhonghui Zhang, Zhichao Liu, Yang Tian

zcliu@chem.ecnu.edu.cn (Z.L.)
ytian@chem.ecnu.edu.cn (Y.T.)

HIGHLIGHTS

A DNA-based FLIM reporter was developed for tracking lysosomal pH and Ca^{2+}

It was found that autophagy could be induced by lysosomal pH and Ca^{2+}

Aβ-induced neuronal death was due to pH_{ly}- and $[Ca^{2+}]_{ly}$-mediated autophagy abnormal

Antiaging-related transformation of qNSCs can be regulated by pH_{ly} and $[Ca^{2+}]_{ly}$

Zhang et al., iScience *23*, 101344
July 24, 2020
https://doi.org/10.1016/j.isci.2020.101344

iScience

CellPress
OPEN ACCESS

Article

A DNA-Based FLIM Reporter for Simultaneous Quantification of Lysosomal pH and Ca^{2+} during Autophagy Regulation

Zhonghui Zhang,[1,2] Zhichao Liu,[2,*] and Yang Tian[1,2,3,*]

SUMMARY

pH and Ca^{2+} play important roles in regulating lysosomal activity and lysosome-mediated physiological and pathological processes. However, effective methods for simultaneous determination of pH and Ca^{2+} is the bottleneck. Herein, a single DNA-based FLIM reporter was developed for real-time imaging and simultaneous quantification of pH and Ca^{2+} in lysosomes with high affinity, in which a specific probe for recognition of Ca^{2+} was assembled onto a DNA nanostructure together with pH-responsive and lysosome-targeted molecules. The developed DNA reporter showed excellent biocompatibility and long-term stability up to ~56 h in lysosomes. Using this powerful tool, it was discovered that pH was closely related to Ca^{2+} concentration in lysosome, whereas autophagy can be regulated by lysosomal pH and Ca^{2+}. Furthermore, Aβ-induced neuronal death resulted from autophagy abnormal through lysosomal pH and Ca^{2+} changes. In addition, lysosomal pH and Ca^{2+} were found to regulate the transformation of NSCs, resulting in Rapamycin-induced antiaging.

INTRODUCTION

Lysosomes are mainly acidic organelles that regulate cellular processes including catabolism by digestion and transmission of proteins, autophagy by the fusion of lysosomes and autophagosomes as well as apoptosis by releasing cathepsin (Settembre et al., 2013; Luzio et al., 2007). Lysosomal dysfunction is of vital importance for the pathology of common neurodegenerative diseases and aging (Li et al., 2018; Tian et al., 2016; Yang et al., 2017). The changes of pH and Ca^{2+} in lysosomes play important roles in lysosome-mediated physiological and pathological processes (Bagh et al., 2017; Shen et al., 2012). Under physiological conditions, pH value in lysosome is around 4.5 (Pan et al., 2016). This acidic environment of lysosome not only is crucial to maintain the proton gradient, which affects the permeability of lysosomal membranes toward different ions, like Ca^{2+}, but also regulates the activity of lysosomes, which influences the formation of autolysosomes (Wan et al., 2014; Chung et al., 2019). Moreover, lysosome as significant "calcium pool" in live cells takes momentous roles in maintaining Ca^{2+} homeostasis as well as signal transduction (Zhu et al., 2016). For example, excessive reduction of Ca^{2+} concentration in lysosome leads to lysosomal dysfunction, resulting in malfunction of cellular uptake and excretion, and further causes autophagy dysfunction and aging. Therefore, it is very important to monitor the changes of pH and Ca^{2+} in the lysosome.

Over the past decades, several elegant methods have been developed for the detection of either pH or Ca^{2+} in lysosome (Pan et al., 2016; Wan et al., 2014; Tang et al., 2009; Egawa et al., 2011; Dong et al., 2016; Minamiki et al., 2019; Li et al., 2015). Previous work has also reported a pH-corrected measurement of Ca^{2+} concentrations in lysosomes, which was realized by calculation (Christensen et al., 2002; Narayanaswamy et al., 2019). Our group has been committed to develop analytical methods for determination of metal ions and oxidative stress-related biological species in live cells and brain (Zhu et al., 2012; Kong et al., 2011, 2012; Liu et al., 2017, 2018a, 2018b, 2019a, 2019b; Li et al., 2017a; Wang et al., 2019a). Recently, we have developed a ratiometric nanosensor to detect pH value and Ca^{2+} concentration in mitochondria (Liu et al., 2018a, 2018b). However, it is still hard to simultaneously perform imaging and biosensing of pH value and concentration of Ca^{2+} in lysosome because simultaneous detection of multiple substances may be affected by the fluorescence resonance energy transfer (FRET) or cross talk (Shcherbakova et al., 2018). Meanwhile, multiple substances detection requires the same localization, same fluorophore concentration ratios, which are hard to realize. In addition, imaging and biosensing of lysosomal pH and Ca^{2+} require high

[1]State Key Laboratory of Precision Spectroscopy, East China Normal University, Dongchuan Road 500, Shanghai 200241, China

[2]Shanghai Key Laboratory of Green Chemistry and Chemical Processes, School of Chemistry and Molecular Engineering, East China Normal University, Dongchuan Road 500, Shanghai 200241, China

[3]Lead Contact

*Correspondence: zcliu@chem.ecnu.edu.cn (Z.L.), ytian@chem.ecnu.edu.cn (Y.T.)

https://doi.org/10.1016/j.isci.2020.101344

spatial and temporal resolution since lysosomes are only ~0.5 μm, much smaller than other organelles (Omen et al., 2019). Stability is also a difficulty to be considered because of the strong digestion ability of lysosomes. Therefore, it is a challenging work to realize simultaneous quantification of multiple substances using a single probe in lysosomes.

To break through the above difficulties, a single FLIM-based DNA reporter was created for simultaneous imaging and real-time quantification of pH and Ca^{2+} in lysosome with high spatial and temporal resolutions (Figure 1A). Taking advantage of DNA nanostructure, including controllable size and shape as well as excellent biocompatibility (Song et al., 2010; Lin et al., 2016; Li et al., 2017a, 2017b; Zhang et al., 2001), the designed highly specific Ca^{2+} probe, pH-responsive probe, and lysosome-targeted molecules were co-assembled onto the vertexes of bipyramid-DNA (bDNA) to form a single nanoprobe with high stability and selectivity. On the other hand, fluorescence lifetime imaging microscopy (FLIM) provides a powerful methodology for accurate biosensing and bioimaging with high spatial resolution at single cell level, which is usually independent of fluorophore concentrations, light sources, environmental changes, and spectral overlap between different fluorophores (Fan et al., 2018; Kawai et al., 2004). Therefore, the developed FLIM-based DNA reporter with long-term stability and good biocompatibility was successfully applied for simultaneous imaging and biosensing of lysosomal pH and Ca^{2+} in single neural cell. Using the developed DNA reported, we found that th epH value increased with decreasing concentration of Ca^{2+} in lysosome, and vice versa. More importantly, it was discovered that autophagy can be regulated by lysosomal pH and Ca^{2+}. Furthermore, Aβ-induced neuronal death was found to be ascribed to abnormal autophagy, which was regulated by lysosomal pH and Ca^{2+}. Moreover, the relationship between aging and lysosomal pH and Ca^{2+} was further explored; it was found that aging-related qNSCs activation can also be controlled by improving lysosomal pH and reducing the concentration of Ca^{2+} in lysosomes.

RESULTS

Assembly and Characterization of DNA Reporter

The lysosome-targeted DNA reporter for simultaneous determination of pH and Ca^{2+} was designed as four parts: a specific element for recognition of Ca^{2+}–fluorescent carbon dots conjugated with calcium ligand (gCD@CaL), pH-responsive Rhodamine B (RhB), lysosome-targeted 2-(4-morpholinyl) ethyl isothiocyanate (MP), and a bipyramidal DNA (bDNA) nanostructure with principal axis length of ~14 nm. The recognition elements for Ca^{2+} and pH together with MP were assembled and conjugated onto the bDNA through chemical bonds, as shown in Figure 1A. As a starting point of this work, gCDs were prepared from m-phenylenediamine by hydrothermal synthesis according to the previous report (Jiang et al., 2015). From transmission electron microscopy (TEM) image shown in Figure 1B, the diameter of gCDs was estimated to 3.00 ± 0.25 nm (n = 100). The high-resolution TEM image demonstrated the typical lattice spacing of gCDs was 0.21 nm, consistent with the in-plane lattice spacing of graphene (100) (Jiang et al., 2015). Meanwhile, atomic force microscope (AFM) image proved that gCDs were monodispersed with average height of 1.25 ± 0.06 nm (n = 100, Figure S1A). On the other hand, the ligand for specific recognition of Ca^{2+}, CaL, was designed and synthesized (Scheme S1; Data S1). The dissociation constant (K_d) of CaL for Ca^{2+} was calculated to be 346 ± 17 μM (n = 5), indicating CaL has a strong coordination effect on Ca^{2+}. Then, CaL was conjugated onto the surface of gCDs to form gCD@CaL through Schiff base reaction between $-NH_2$ group of gCDs (1,048 cm^{-1}) and -CHO group of CaL (~1,725 cm^{-1} and ~3,039 cm^{-1}). As shown in Figure 1C, after gCD@CaL was formed, a new peak located at ~1,640 cm^{-1} was observed, which belongs to the stretching vibration of C=N. It should be pointed out that, after gCD@CaL was incubated with buffer solutions of different pH (pH = 3.00, 4.01, 5.00) for 56 h, negligible changes (<1.0%) at ~1,640 cm^{-1} ($\upsilon_{C=N}$) were observed for gCD@CaL (Figure S1B). These results prove that CaL was successfully conjugated onto gCDs with high stability. Moreover, UV-vis absorption spectrum of gCDs shows well-defined absorption peaks at 214, 296, and 356 nm, which were attributed to π-π* and n-π* transition, respectively. After CaL was conjugated onto gCDs, the absorption bands of gCDs@CaL red-shifted, from 214 to 254 nm, 295 to 313 nm, and 351to 364 nm (Figure 1D). Meanwhile, the fluorescent intensity of gCDs was decreased and the fluorescent lifetime was shortened (Figures 1D and S2G), clearly demonstrating that the electrons of gCDs transferred to CaL ligands after the successful production of gCD@CaL probe.

Then, a bDNA nanostructure was designed and prepared with different functional groups ($-NH_2$ or -CHO) for further assembling gCD@CaL, RhB, and MP (Erben et al., 2007). From bio-fast AFM images (Figure S1D), a uniform distribution of bDNA with a typical bipyramidal morphology can be observed. Polyacrylamide gel electrophoresis (PAGE) results also suggest the high generation yield of bDNA. Meanwhile, RhB or

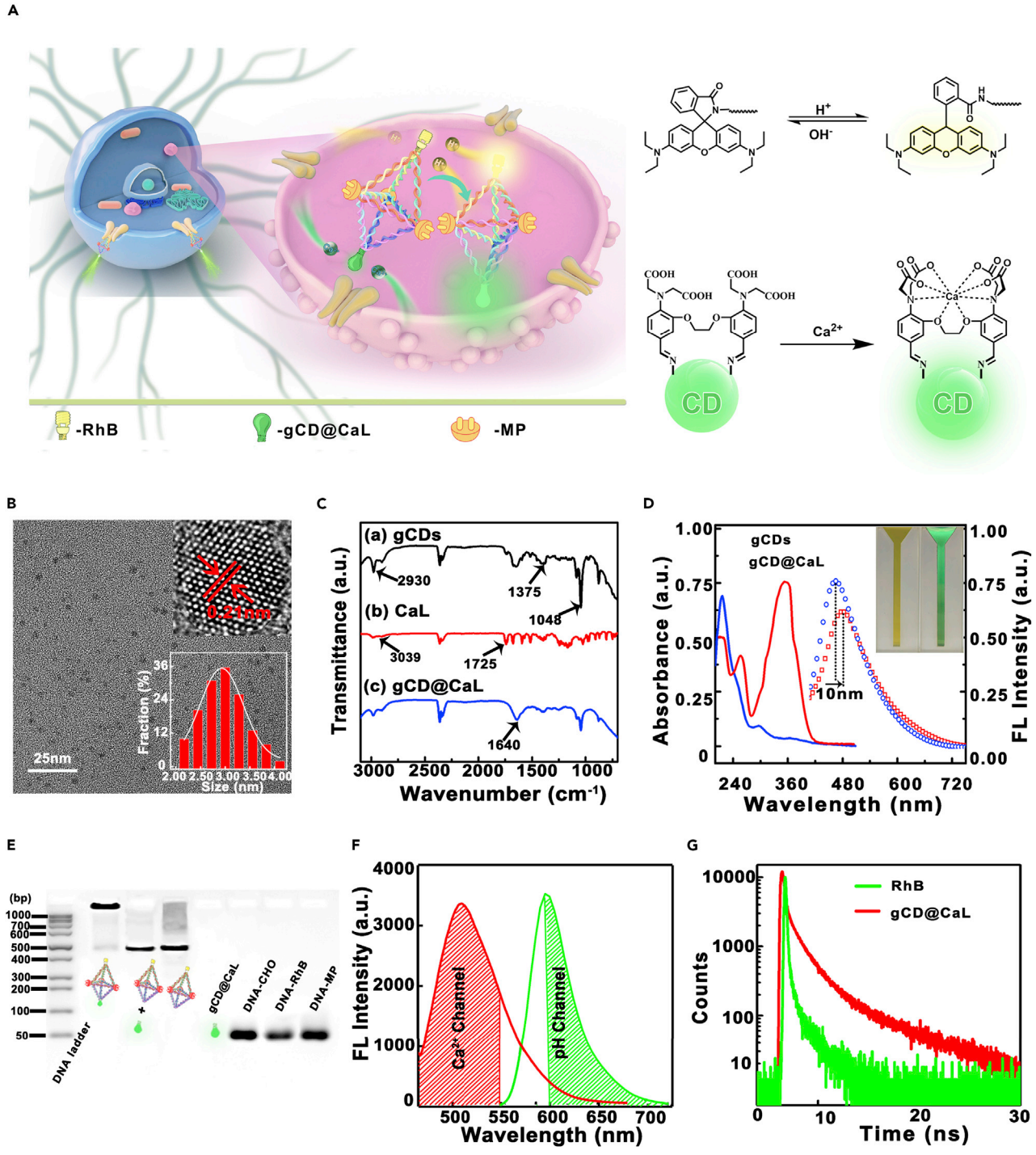

Figure 1. Synthesis and Characterization of DNA Reporter

(A) Schematic illustration for the working principle of the developed DNA reporter for simultaneous determination of pH and Ca^{2+} in lysosome.

(B) TEM image of gCDs. Insets depict high-resolution TEM image and diameter distribution of gCDs.

(C) FTIR spectra of gCDs, CaL, and gCD@CaL.

(D) UV-vis absorption spectra and fluorescence emission spectra of gCDs and gCD@CaL under 405 nm excitation.

(E) Agarose electrophoresis analysis of DNA reporter. From left to right: DNA ladder (50–1,000 bp), DNA reporter, the mixture of gCD@CaL and bDNA-MP + RhB, bDNA-MP + RhB, gCD@CaL, DNA-CHO (aldehyde group), DNA-RhB, and DNA-MP, respectively.

(F) The threshold for fluorescent channels of RhB and gCD@CaL at excitation wavelength of 405 nm.

(G) Fluorescent lifetime decays of pH probe (RhB) and Ca^{2+} probe (gCD@CaL) collected from different channels.

MP-labeled DNA strands (DNA-RhB, DNA1-MP, DNA2-MP and DNA3-MP) were synthesized (Figures S1C, S1E, and S1F) to produce bDNA-MP + RhB probe. Finally, gCD@CaL, MP, and RhB were successfully assembled onto bipyramidal DNA nanostructure to generate DNA reporter, bDNA-MP + RhB + gCD@CaL, for simultaneous determination of pH and Ca^{2+}, which was confirmed by agarose electrophoresis as shown in Figure 1E. In addition, dynamic light scattering (DLS) results show that the average diameter of individual gCD@CaL and bDNA-MP + RhB probes were 17.82 $\pm$ 5.00 and 63.64 $\pm$ 6.02 nm (n = 5), respectively. After gCD@CaL was assembled onto bDNA-MP + RhB, the average diameter of the produced bDNA-MP + RhB + gCD@CaL probe was increased to 79.22 $\pm$ 7.04 nm (n = 5, Figure S1G). Furthermore, in order to confirm the conjugated number of gCD@CaL on each bipyramidal DNA unit, TEM was used to characterize the assembled DNA reporter. The assembly of gCD@CaL with bDNA-MP + RhB produced monodispersed and disordered gCD@CaL (Figure S1H), but it is difficult to observe the conjugated number of gCD@CaL on each bipyramidal DNA unit. Subsequently, a new bDNA-1 with two bare -CHO groups on vertices was prepared and further used to assemble with gCD@CaL. As shown in Figure S1I, two gCD@CaL particles were assembled onto bDNA-1. The distance between these two gCD@CaL particles was estimated about 14 nm from TEM image, which was consistent with the distance of the vertex of bDNA-1. All these results proved the successful assembly of bDNA-MP + RhB + gCD@CaL probe.

Simultaneous Determination of pH and Ca^{2+} Using the Developed DNA-Based FLIM Reporter

The analytical performance of the DNA reporter for simultaneous sensing of pH and Ca^{2+} was evaluated. As shown in Figure 1F, gCD@CaL and RhB assembled onto DNA nanostructure showed emission peaks located at 514 and 583 nm under excitation of 405 nm, respectively. Meanwhile, the average fluorescence lifetimes of gCD@CaL and RhB were estimated to be 0.96 ns (1.86 ns, 41%; 0.33 ns, 59%) and 2.85 ns (3.44 ns, 78.5%; 0.70 ns, 21.5%), as demonstrated in Figure 1G, from Equations (1) and (2) when the signals were collected from 450–550 and 610–700 nm, respectively. Thus, the average lifetime of RhB and gCD@CaL in the DNA reporter can be distinguished clearly.

$$\overline{\tau} = \frac{\sum_{i=1}^{2} \alpha_i \tau_i^2}{\sum_{i=1}^{2} \alpha_i \tau_i} \quad \text{(Equation 1)}$$

$$f_i = \frac{\alpha_i \tau_i}{\sum_i \alpha_i \tau_i} \quad \text{(Equation 2)}$$

where τ_i is the lifetime, α_i is the fractional amplitude with $\sum \alpha_i = 1$, f_i is the fractional intensity of each decay time to the steady-state intensity, and $\overline{\tau}$ is the average fluorescence lifetime of the probe.

With increasing concentration of Ca^{2+}, the fluorescence lifetime of gCD@CaL channel (450–550 nm) was prolonged from 2.92 to 7.83 ns as demonstrated in Figure 2A, accompanied with fluorescent enhancement (Figures S2A and S2B). As summarized in Figure 2B, the average fluorescence lifetime of gCD@CaL channel displayed a good linearity with Ca^{2+} concentration in the range of 10–600 μM. The detection limit was calculated to be 2.53 $\pm$ 0.04 μM (S/N = 3, n = 5). This Ca^{2+}-induced fluorescence enhancement and lifetime prolongation of gCD@CaL can be attributed to the inhibition of electron transfer process between CaL and gCDs. In the absence of Ca^{2+}, gCD@CaL showed clear absorption peaks at 254, 288, 313, and 364 nm. The absorption bands of gCD@CaL had red-shifts compared with those of gCDs, which were attributed to the electrons of gCDs transferred to CaL ligands. However, with the increasing concentrations of Ca^{2+}, the absorption peak at 364 nm of gCD@CaL was decreased, whereas the absorption peak at 288 nm blue-shifted to 282 nm (Figures S2E and S2F), together with the fluorescence recovery of gCD@CaL. (Figure 2A). These results demonstrated that, after gCD@CaL was conjugated with Ca^{2+}, the electron transfer from gCDs to CaL was inhibited. Moreover, the electron transfer between gCDs and CaL was proved by transient absorption spectroscopy (TAS) (Sakamoto et al., 2005; Tachikawa et al., 2007). As for gCDs, a negative absorption band with peak at 500 nm and a broad positive absorption band with peak at 640 nm were observed, which were attributed to stimulated emission (SE) and excited state absorption (ESA), respectively (Figure S2H). However, after gCDs were conjugated with CaL to form gCD@CaL, the peak at 500 nm had an apparent decrease, indicating that electrons of gCDs were transferred to CaL, resulting in the decrease of stimulated emission (Figure S2I). More interestingly, with the addition of Ca^{2+}, the peak at 500 nm was correspondingly recovered, which should be contributed to the inhibition of electrons transformation from gCDs to CaL (Figure S2J). Furthermore, the TA (transient absorption) kinetic traces were recorded at 640 nm. As shown in Figure S2K, two distinct signals for the lifetimes of gCDs were 3.31 and 36.82 ps, indicating two excitation pathways were observed for fluorescence emissions of gCDs. Meanwhile, the lifetime of gCDs@CaL became 7.18 and 185.36 ps after CaL was conjugated onto gCDs, indicating that conjugation of CaL

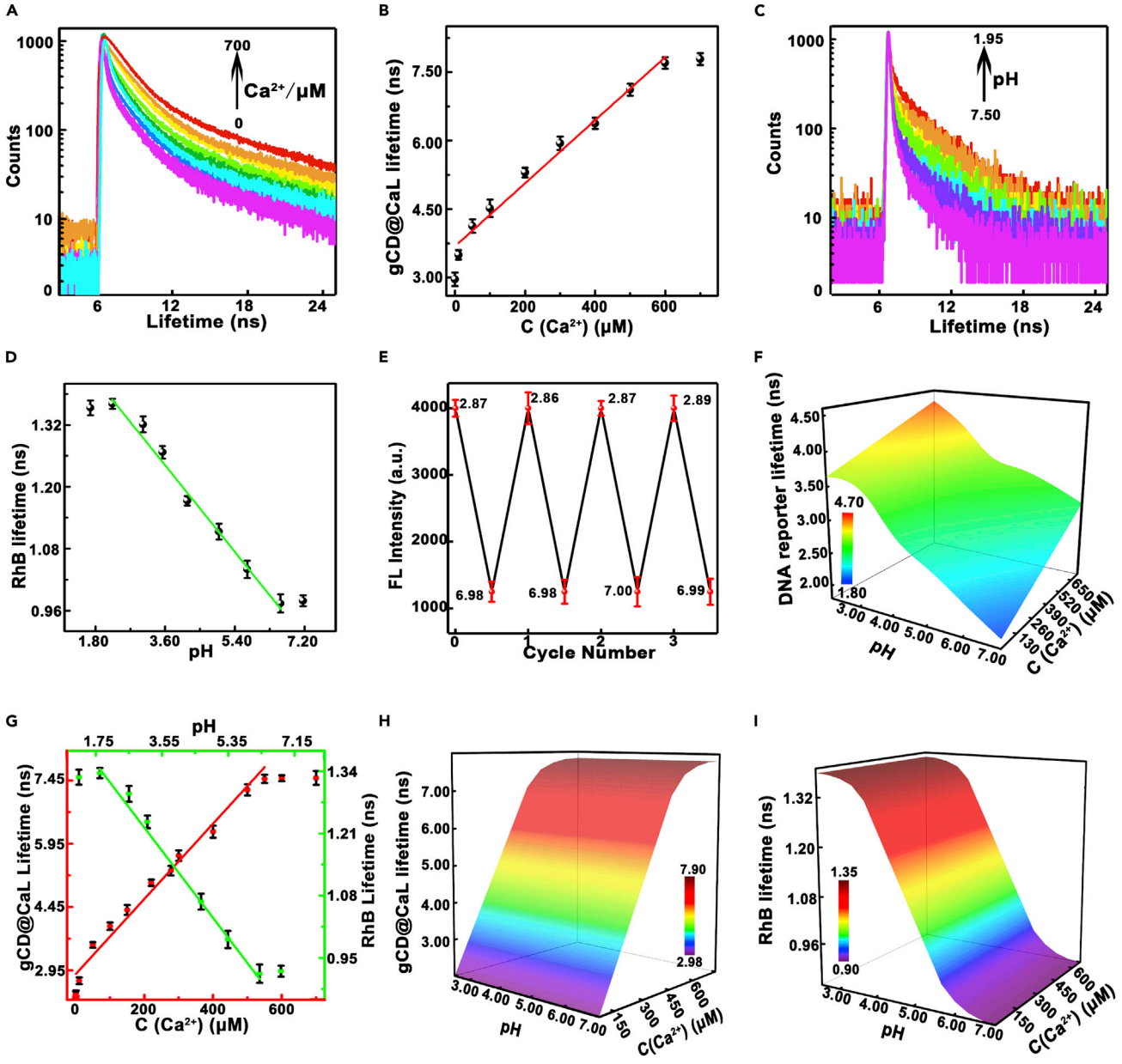

Figure 2. Analytical Performance of the DNA Reporter for Simultaneous Determination of Ca^{2+} and pH

(A) Fluorescence lifetime decay curves of gCD@CaL in the presence of various concentrations of Ca^{2+} (0, 1, 5, 10, 50, 100, 200, 300, 400, 500, 600, and 700 μM).

(B) Calibration curve between average fluorescence lifetime of gCD@CaL and various concentrations of Ca^{2+} in (A).

(C) Fluorescence lifetime decay curves of RhB in the presence of different pH values (1.95, 2.09, 3.29, 4.10, 5.02, 6.09, 6.58, 7.00, 7.50).

(D) Calibration curve between average fluorescence lifetime of RhB and different pH in (C).

(E) Fluorescence reversibility responses of RhB between pH 2.80 and 7.00.

(F) Average fluorescence lifetime of the reporter obtained at excitation wavelength of 405 nm at different pH values (1.95, 2.09, 3.29, 4.10, 5.02, 6.09, 6.58, 7.00, 7.50) in the presence of different concentrations of Ca^{2+} (0, 1, 5, 10, 50, 100, 200, 300, 400, 500, 600, and 700 μM).

(G) Calibration curve between average fluorescence lifetime of gCD@CaL and RhB at different pH values in the presence of different concentrations of Ca^{2+} in (F).

(H) 3D surface plot of gCD@CaL channel lifetime response as a function of Ca^{2+} concentration and pH.

(I) 3D surface plot of RhB channel lifetime as a function of Ca^{2+} concentration and pH. Data are expressed as mean ± SD of five samples in each experimental group.

onto gCDs caused a new decay pathway in the excited-state relaxation. This new decay pathway resulted from the electron transfer between CaL and gCDs. However, with the addition of 100 μM Ca^{2+}, the lifetimes of gCDs@CaL signals changed back, implying electron transfer-related new decay pathway in the excited-state relaxation was inhibited.

Similarly, the average fluorescence lifetime of RhB channel (610–700 nm) was prolonged from 0.92 ns to 1.33 ns with decreasing pH from 7.50 to 1.95 (Figure 2C). The increase in the fluorescence intensity of RhB was also observed (Figures S2C and S2D). The average fluorescence lifetime of RhB showed a good linear relationship with pH value from 2.24 to 6.58, and pK_a was calculated to be 3.58 ± 0.82 (n = 5, Figure 2D), which is very beneficial for pH sensing in lysosome. It is mentioned that RhB molecule shows an emission peak around 515 nm, which is attributed to the emission of xanthine part of RhB. Under alkaline conditions, the molecule maintains a spiral loop state condition. However, the delocalization of electrons in xanthene was enhanced after addition of H^+, and the structure of RhB changed from spirocyclic (non-fluorescent) to ring-open (fluorescent) forms (Shen et al., 2015). In addition, RhB shows a good reversibility when pH changed between 7.00 and 2.80 (Figure 2E).

More importantly, the DNA reporter was used for simultaneous determination of pH and Ca^{2+}. The average fluorescence lifetime of the developed DNA reporter gradually prolonged with increasing concentration of Ca^{2+} from 0.2 to 700 μM as well as decreasing pH value from 7.50 to 1.95. Because the fluorescence emission spectra for gCD@CaL and RhB channels were well separated (Figure 1F), the lifetimes with the fluorescent spectra of gCDs@CaL and RhB channels were collected from 450 to 550 nm and 610 to 700 nm. The average fluorescence lifetime of gCD@CaL channel displayed a good linearity with Ca^{2+} concentration in the range of 10–650 μM as demonstrated in Figure 2G, and the detection limit was estimated to be 2.36 ± 0.07 μM (S/N = 3, n = 5), as summarized in Equation (3):

$$\tau_{gCD@CaL} = 0.00777 \times \left[Ca^{2+}\right] + 3.13956 \quad \text{(Equation 3)}$$

Similarly, the average fluorescence lifetime of RhB channel displayed a good linearity with pH from 2.25 to 6.70 (Figure 2G), and pK_a was calculated to be 3.37 ± 0.62 (n = 5), as summarized in Equation (4):

$$\tau_{RhB} = -0.104 \times pH + 1.6266 \quad \text{(Equation 4)}$$

Moreover, this nanoprobe also showed rapid response dynamics toward pH and Ca^{2+}. The response times for 1.0 pH and 200 μM Ca^{2+} were estimated to be 2 and 4 s, respectively (Figure S2L). Furthermore, there are no cross talk or fluorescence resonance energy transfer (FRET) between RhB and gCD@CaL assembled onto DNA nanostructure (Figures 2H and 2I).

Since the environment in live cells is complicated, the selectivity of the developed DNA reporter was also tested against potential biological species including metal ions, reactive oxygen species (ROS), and amino acids. No obvious responses (<2.9%) were observed on the channels of RhB and gCD@CaL (Figures S3A–S3F) for metal ions such as K^+ (50 mM), Na^+ (100 mM), Mg^{2+} (300 μM), Al^{3+}, Zn^{2+}, Ni^{2+}, Co^{2+}, Fe^{3+}, and Cu^{2+} (10 μM); amino acids; and ROS including H_2O_2, $O_2^{\bullet-}$, $^1O_2$, and •OH. Moreover, in the competition tests, negligible effects of other metal ions, amino acids, and ROS were obtained for the responses of RhB and gCD@CaL channels (<3.2%) in the developed probe. All these results demonstrated that the developed FLIM reporter showed high selectivity and accuracy, as well as quick response, which was very powerful for real-time sensing and simultaneous quantifying of pH and Ca^{2+} in live cells.

The Stability, Biocompatibility, and Accuracy of the Developed DNA Reporter

For further application, the stability of the developed DNA reporter was also estimated. Lysosomes as acid organelles, which contain many hydrolytic enzymes, can easily degrade substances and probes (Wang et al., 2019b). The stability of the DNA reporter in lysosome was also estimated, and the ability of the developed nanoprobe for targeting lysosome was first investigated. Co-localization imaging results showed that the fluorescence of developed nanoprobe merged well with that of commercialized lysosomal dye (LysoTracker green) both in neurons and stem cells. Pearson's correlation coefficients were calculated as 0.92 and 0.94 in neurons and stem cells, respectively (Figure 3A), suggesting that the present probe was mainly located in lysosome. In addition, no obvious change (<2.0%) was obtained for the fluorescent intensity of gCD@CaL even after the DNA reporter entered into lysosomes for 56 h (Figures S3M and S3N). Moreover, the fluorescence lifetime signals of the developed nanoprobe remained stable (<8.5%) in lysosomes and the DNA reporter showed high structural stability even after the nanoprobe was incubated with cells for

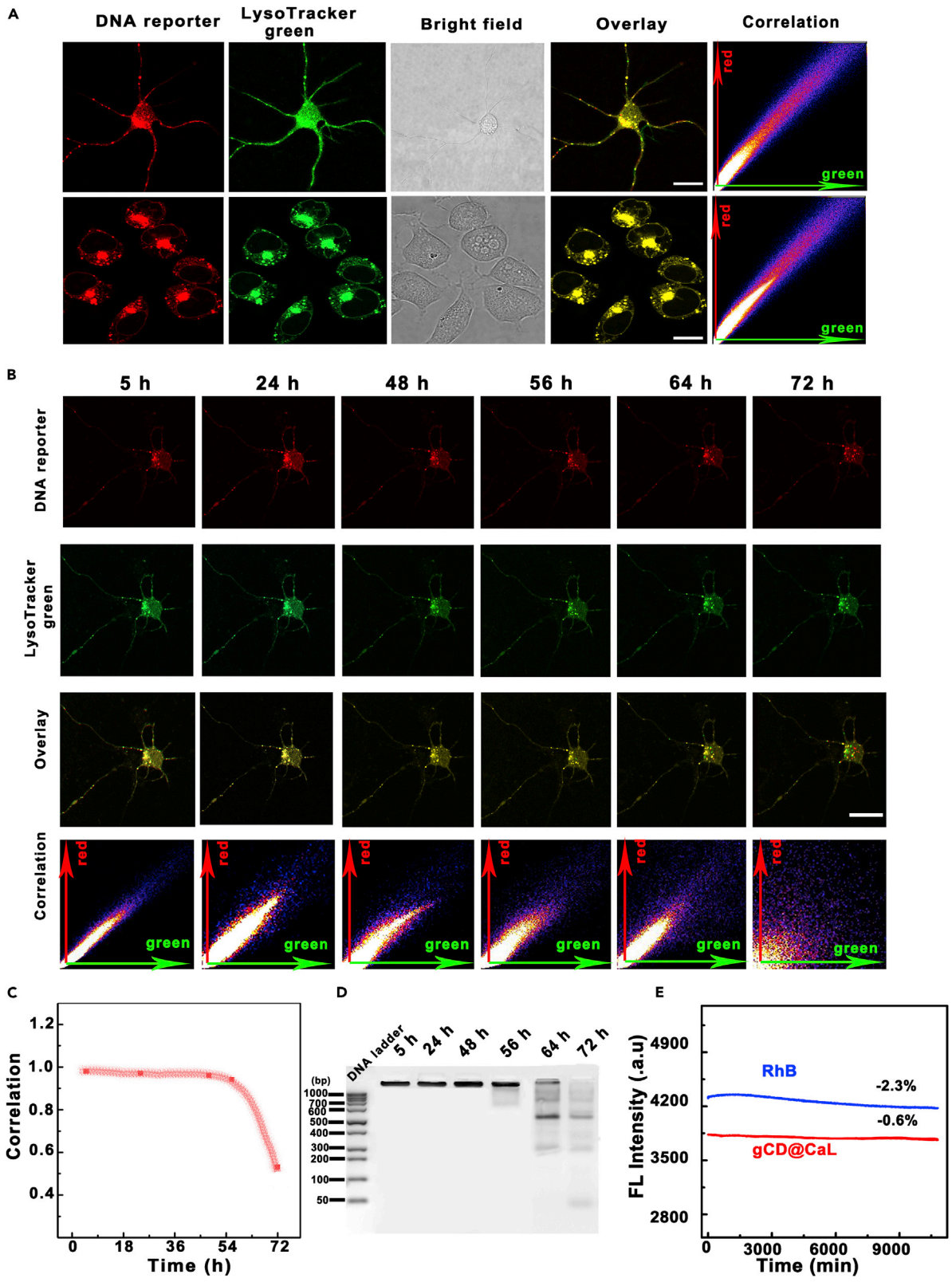
A
DNA reporter
LysoTracker green
Bright field
Overlay
Correlation
red
green
B
5 h
24 h
48 h
56 h
64 h
72 h
DNA reporter
LysoTracker green
Overlay
Correlation
C
Correlation
Time (h)
D
DNA ladder
(bp)
1000
700
600
500
400
300
200
100
50
E
FL Intensity (a.u)
Time (min)
RhB
gCD@CaL
-2.3%
-0.6%

Figure 3. Intracellular Stability of the Developed Nanoprobe

(A) Confocal fluorescence images of neurons and stem cells treated with the developed nanoprobe and LysoTracker Green. Scale bar: 15 μm.

(B) Confocal fluorescence images of neurons treated with the present nanoprobe and LysoTracker Green for different times (5, 24, 48, 56, 64, 72 h). Scale bar: 10 μm.

(C) The colocation correlation of neurons treated with the present nanoprobe and LysoTracker Green.

(D) Agarose electrophoresis (2%) analysis of DNA reporter incubated with neurons for different times (5, 24, 48, 56, 64, 72 h).

(E) Normalized fluorescence intensity of RhB and gCD@CaL obtained from DNA Reporter upon exposure to Xe lamp (90 W). Data are expressed as mean ± SD of five samples in each experimental group.

56 h, which fulfills the requirement for cell experiments. However, the overall signals of the developed nanoprobe in lysosomes decreased to 54%, and the pH channel and gCD@CaL channel signals decreased to 52% and 58%, respectively, after they were incubated with cells for 72 h (Figures 3B and 3C). Meanwhile, the DNA structure was observed to keep stable within 56 h (94%) and then gradually degraded for about 48% at 72 h (Figure 3D). Furthermore, after the assembled DNA reporter was exposed to a Xe lamp (90 W) for 2.5 h, no obvious photobleaching was observed from both signals of gCD@CaL and RhB channels (<3.8%), which fulfills the requirement for cell experiments (Figure 3E). All these results demonstrated that the assembled DNA reporter showed high structural stability and long-term photostability.

Before imaging and biosensing of lysosomal pH and Ca^{2+}, the cytotoxicity and biocompatibility of the developed DNA reporter were first evaluated. MTT results showed that the cell viability was higher than 92% even after the nanoprobe (25 μM) was incubated with cells for 48 h; this concentration of nanoprobe was higher than that used in live cells (Figures S3G and S3H). In addition, fluorescence-activated cell sorting (FACS) results confirmed that no obvious differences were observed for live cells, viable apoptotic cells, late apoptotic cells, and non-viable cells after the cells were incubated with different concentrations of the developed nanoprobe (Figures S3I and S3J), proving good biocompatibility of the developed fluorescent probe. The low cytotoxicity and good biocompatibility of this nanoprobe was attributed to the presence of non-toxicity DNA framework and biocompatible gCDs.

Meanwhile, the commercial lysosomal pH probe (DND-189) was employed to calibrate the accuracy of our developed method. As shown in Figures S3K and S3L, the fluorescence intensity of DNA-189 displayed a good linearity with pH from 2.93 to 6.09, and pKa was calculated to about 5.2, as summarized in Equation (5):

$$F = -200.025 \times pH + 1442.90 \quad \text{(Equation 5)}$$

In addition, the average fluorescence lifetime of RhB also showed a good linearity with pH from 2.24 to 6.58, which obeys Equation (4).

Then, T test method was used to compare the determined results from the commercial probe and those from our developed nanoprobe. As summarized in Table S2, no significant difference was obtained between two probes. These results proved that the developed nanoprobe showed the same accuracy with the commercial probe.

Real-Time Tracking and Simultaneous Quantification of Lysosomal pH and Ca^{2+} Regulating the Level of Autophagy in Single Neuron

Taking the advantages of the developed nanoprobe, including high selectivity and accuracy, as well as long-term stability, the developed FLIM nanoprobe was applied for monitoring the levels of lysosomal pH and Ca^{2+} (pH_{ly} and $[Ca^{2+}]_{ly}$) in neurons. As shown in Figure 4A, under physiological conditions, lysosomal pH value and Ca^{2+} concentration were estimated to be 4.83 ± 0.03 and 525 ± 17 μM (n = 100), respectively. With increasing extracellular pH value from 4.00 to 6.70, the fluorescence lifetime of overall channel was shortened. The lysosomal pH was increased from 4.00 ± 0.24 to 6.70 ± 0.13 (n = 100). Interestingly, the concentration of lysosomal Ca^{2+} was also decreased from 611 ± 18 to 31 ± 2 μM (n = 100) (Figures 4B–4G). It should be pointed out that no obvious change was observed for pH_{ly} or $[Ca^{2+}]_{ly}$ at pH 6.70 in the absence of nigericin. These results proved that the increase of pH_{ly} caused the decrease of $[Ca^{2+}]_{ly}$ concentration. On the other hand, after neurons were treated with EGTA, a chelator for Ca^{2+}, the concentration of lysosomal Ca^{2+} was, as expected, decreased to 180 ± 11 μM (n = 100). However, lysosomal pH was found to be increased to 5.42 ± 0.27 (n = 100) (Figure 4H). These results demonstrated that lysosomal pH was closely related to the concentration of Ca^{2+}, that is, the concentration of lysosomal Ca^{2+}

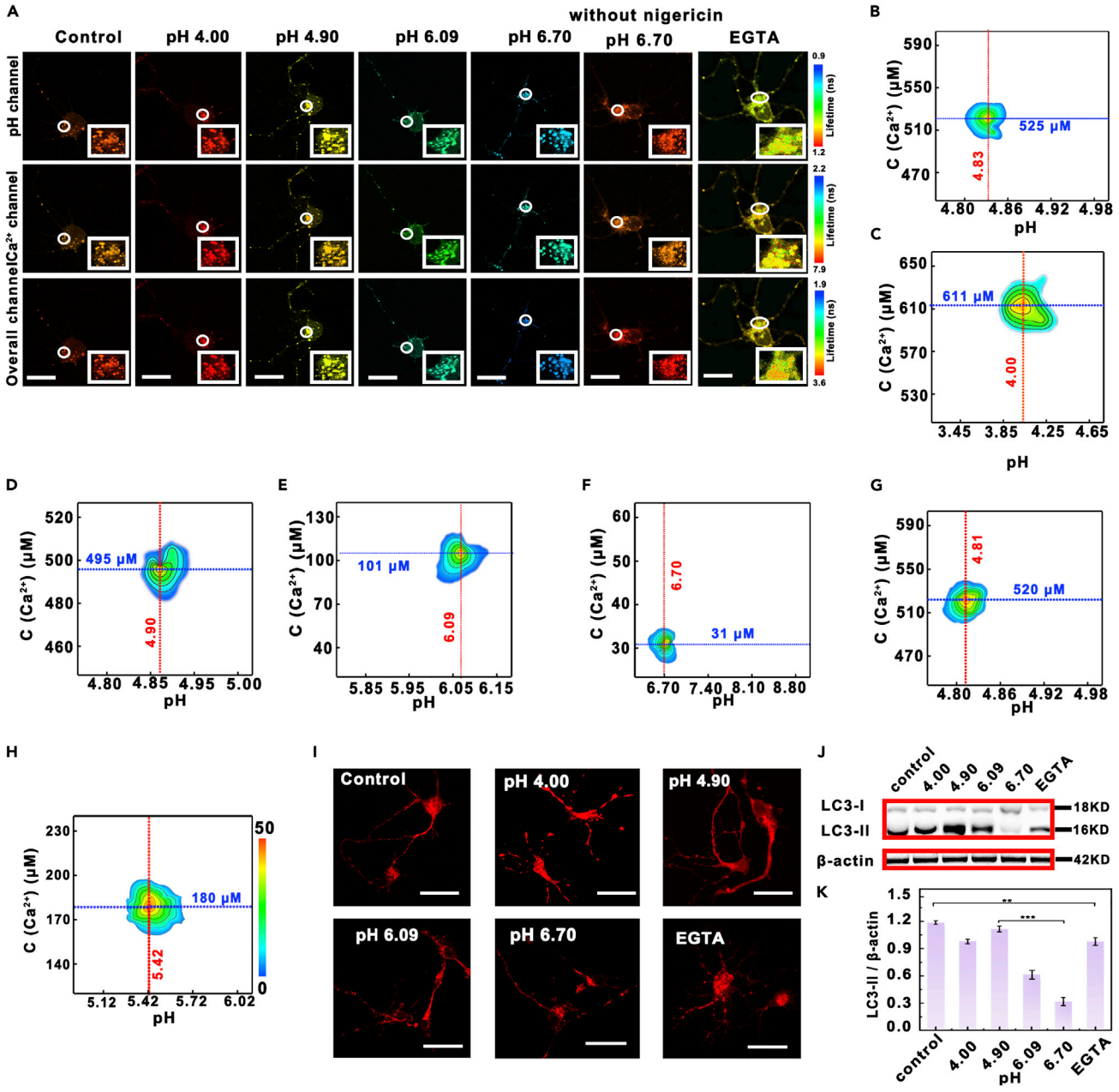

Figure 4. Co-localization Imaging and Fluorescence Lifetime Imaging of Lysosomal pH and Ca^{2+} in Neurons

(A) Confocal fluorescence lifetime images of neurons collected from pH channel, Ca^{2+} channel, and overall channel treated with the present nanoprobe at different pH values (4.00, 4.90, 6.09 6.70, 6.70 without nigericin) and in the presence of EGTA, respectively. Scale bar: 15 μm.

(B–H) Lysosomal density scatter profiles of neurons at (B) control, (C) pH 4.00, (D) pH 4.90, (E) pH 6.09, (F) pH 6.70, (G) 6.70 without nigericin, and (H) in the presence of EGTA. The density plot was pseudo color, where red and blue correspond to populations with higher and lower frequencies of occurrence. The data were obtained from 100 lysosomes in ten cells.

(I) Fluorescence images of neurons incubated with MDC after lysosomal pH changed from 4.00 to 6.70 in neurons. Scale bar: 30 μm.

(J) Immunoblotting analysis of relative levels of LC3-I and LC3-II in lysate purified from the neurons with different lysosomal pH values.

(K) The quantification of LC3-II/β-actin expression from western blot results. Data are expressed as mean ± SD of five samples in each experimental group. Assume that the significance level of the statistical test is 0.01 (**), and 0.001 (***) (n = 20; **, $p < 0.01$; ***, $p < 0.001$).

was decreased with increasing lysosomal pH. The lysosomal pH also correspondingly went up when the concentration of Ca^{2+} in lysosomes was decreased.

Next, the developed probe was employed to investigate the effects of lysosomal pH and Ca^{2+} on autophagy and further to understand the molecular pathway of autophagy, because autophagy plays important roles in living body. Monodansylcadaverine (MDC) was selected as the fluorescent probe for tracking autophagy level, which can selectively accumulate in autophagic vesicles during autophagy (Biederbick et al., 1995). As shown in Figure 4I, the fluorescence of neurons incubated with MDC gradually increased from pH 4.00 to 4.90 and then decreased from 4.90 to 6.70, indicating that the level of autophagy is closely related to lysosomal pH. The optimized pH value for autophagy was found to be 4.90, which agrees well with that of normal pH in lysosome. Overly acidic (lower than normal pH in lysosome) and basic (higher than normal pH) are all negative to the level of autophagy. More interestingly, the event of autophagy was also weakened when the neurons treated with 10 μM EGTA, a chelator for Ca^{2+}, until $[Ca^{2+}]_{ly}$ decreased from 525 ± 35 to 180 ± 11 μM, suggesting that the level of autophagy was correspondingly decreased with decreasing concentration of Ca^{2+}. Meanwhile, autophagy level was confirmed by the amount of light chain 3 (LC3), a membrane microtubule-associated protein 1. LC3 is the credible biomarker of autophagy, which can lose peptide fragments to produce LC3-I, and the produced LC3-I can bind with phosphatidyl ethanolamine (PE) to form LC3-II during autophagy (Cui et al., 2018; Laraia et al., 2019; Li et al., 2018). As shown in Figures 4J and 4K, the level of LC3-II/β-actin gradually went up from 0.92 ± 0.05 to 1.17 ± 0.06 according to the quantification of western blot as lysosomal pH increased from 4.00 to 4.90. However, the level of LC3-II/β-actin began to decrease and down to 0.32 ± 0.01, after lysosomal pH was continuously increased to 6.70.

On the other hand, after adding chelator for Ca^{2+} (EGTA), the fluorescence of neurons incubated with MDC was decreased compared with those under physiological condition. Meanwhile, the intensity ratio of LC3-II to β-actin was 0.97 ± 0.07 (Figures 4J and 4K), indicating the level of autophagy decreased with decreasing concentration of lysosomal Ca^{2+}. Taken together, these results demonstrated that lysosomal pH and Ca^{2+} greatly contributed to the level of autophagy.

Moreover, it has been reported that bafilomycin A_1 can inhibit the lysosomal proton pump and elevate pH in lysosome, which in turn leads to the decrease of Ca^{2+} concentration in lysosome (Chung et al., 2019). Therefore, the effect of bafilomycin A_1 on lysosomal pH and Ca^{2+} as well as autophagy was further investigated in detail by our accurate probe. It was found that, after the neurons were stimulated by bafilomycin A_1 for 40 min (Figures 5A and S4A), lysosomal pH increased from 4.83 ± 0.05 to 6.73 ± 0.16, whereas lysosomal Ca^{2+} decreased by from 525 ± 35 to 28 ± 3 μM. Meanwhile, the detailed kinetics during the process was also observed. As shown in Figure S4B, lysosomal pH started to increase from 4.83 ± 0.05 after the cells were stimulated by bafilomycin A_1 for 1 min and then quickly increased to 5.37 ± 0.12 in the following 15 min. However, lysosomal Ca^{2+} concentration started to decrease from 525 ± 13 μM after the cells were stimulated by bafilomycin A_1 for 3 min, then decreased to 225 ± 8 μM. In addition, after removing the stimulation of bafilomycin A_1 at 16 min, seldom increasing of lysosomal pH was observed in the following 9 min. It should be pointed out that the lysosomal Ca^{2+} slowly decreased before it tended to stabilize at 218 ± 11 μM in the absence of bafilomycin A_1 stimulation. On the other hand, when the cell culture solution was changed to neurobasal medium and Britton-Robinson (BR) buffer (40 mM) containing 120 mM KCl, 30 mM NaCl, 1 mM NaH_2PO_4, and 5 mM glucose at pH 4.8, lysosomal pH immediately decreased from 5.37 ± 0.19 to 4.85 ± 0.08 within 10 min. Interestingly, the lysosomal Ca^{2+} did not start to change until the pH of the lysosome decreased to 5.25 ± 0.11. All these results proved that the changes of lysosomal Ca^{2+} was induced by pH changing in lysosome. More interestingly, addition of Ca^{2+} channel inhibitor verapamil (VeRa), which can target the α_1 subunit of L-type voltage-gated calcium channel, further inhibits the channel activation and blocks the influx of Ca^{2+} by depolarizing the cell membrane and increasing the threshold potential of calcium channels (Kwon and Triggle, 1991; Rampe and Triggle, 1990; Green et al., 2007), significantly weakening the changes of lysosomal pH and Ca^{2+}. pH_{ly} only increases by 0.67 ± 0.07, whereas $[Ca^{2+}]_{ly}$ only decreased by 25 ± 5 μM after the neurons were stimulated by bafilomycin A_1 for 40 min in the presence of VeRa (Figures 5B–5F).

Meanwhile, as shown in Figure 5G, with the extension of stimulation time by bafilomycin A_1 for 40 min, the fluorescence of neurons incubated with MDC, a tracking marker for autophagy, gradually decreased. More interestingly, in the presence of VeRa, no obvious change was observed after the neurons incubated with MDC. These results demonstrated that, with the extension of the stimulation time of bafilomycin A_1, the

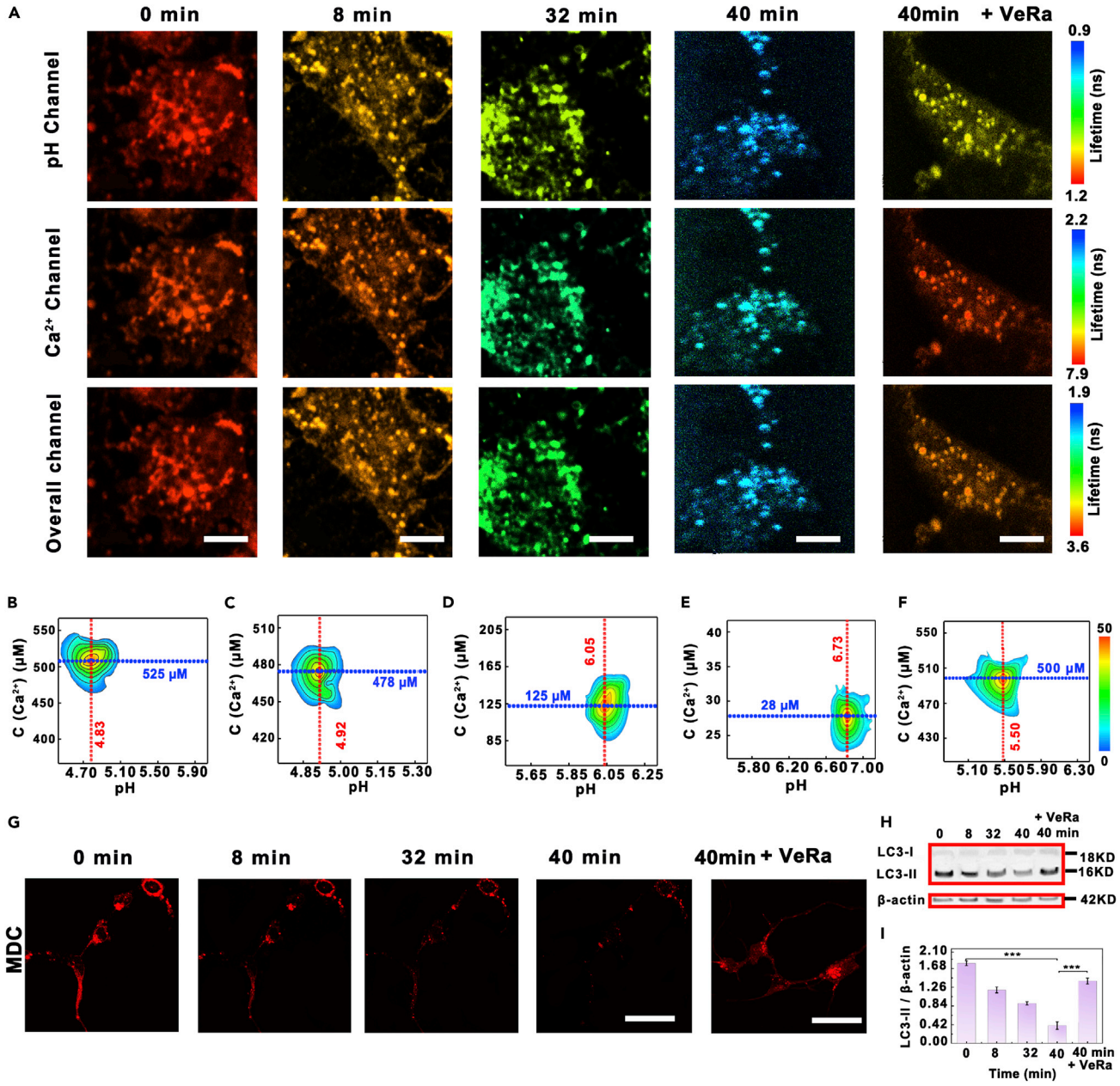

Figure 5. Fluorescence Lifetime Imaging and Quantification of Lysosomal pH and Ca^{2+} in Response to Bafilomycin A_1 in Neurons

(A) Enlarged confocal fluorescence lifetime images of neurons collected from pH channel, Ca^{2+} channel, and overall channel after the neurons were stimulated by 10 μM bafilomycin A_1 for different times (0, 8, 32, 40 min), respectively. For comparison, the image of neurons stimulated by bafilomycin for 60 min in the presence of verapamil was also obtained. Scale bar: 8 μm.

(B–F) Lysosomal density scatter profiles after neurons were stimulated by bafilomycin A_1 for (B) 0, (C) 8, (D) 32, (E) 40, and (F) 40 min in the presence of VeRa. The density plot was pseudo color, here red and blue correspond to populations with higher and lower frequencies of occurrence. The data were obtained from 100 lysosomes in 10 cells.

(G) Fluorescence images of neurons incubated with MDC after the neurons were stimulated by bafilomycin A_1 for different times. Scale bar: 25 μm.

(H) Immunoblotting analysis of relative levels of LC3-I and LC3-II in lysate purified from the neurons that were stimulated by bafilomycin A_1 for different times.

(I) The quantification of LC3-II/β-actin expression from western blot results. Data are expressed as mean ± SD of five samples in each experimental group. Assume that the significance level of the statistical test is 0.001 (***) (n = 20; ***, $p < 0.001$).

level of autophagy was correspondingly decreased. Furthermore, these results were verified using the western blot. As shown in Figure 4H, with the stimulation of bafilomycin A_1, the level of LC3-II was decreased obviously. The intensity ratio of LC3-II to β-actin decreased from 1.71 ± 0.06 to 0.52 ± 0.05 after the neurons were stimulated by bafilomycin A_1 for 40 min, confirming that the level of autophagy was decreased after the neurons were stimulated by bafilomycin A_1 for 40 min. Notably, little decrease (0.04 ± 0.01) of LC3-II was observed after the neurons were stimulated by bafilomycin A_1 for 40 min in the presence of VeRa, demonstrating that VaRa can prevent bafilomycin A_1-induced decreasing of autophagy (Figures 4H and 4I). These results proved that our developed DNA reporter can be used for sensing and quantifying of lysosomal pH and Ca^{2+} in live cells, further indicating that lysosomal pH and Ca^{2+} showed close relationship with the level of autophagy.

Aβ Regulated Autophagy Level by Changing Lysosomal pH and Ca^{2+}

Alzheimer's disease (AD) is a typical neurodegenerative disease, which can be characterized by losing of hippocampal neurons and accumulation of amyloid (Aβ) in the brain. It has been reported that Aβ aggregates disturb lysosomal function and further result in abnormal autophagy (Tian et al., 2016; Yang et al., 2017; Komatsu et al., 2006; Khurana et al., 2010). Thus, we first investigated the neurotoxicity of aggregated $Aβ_{1-42}$, the main component of Aβ plaque. The cell viabilities decreased with the extension of stimulation time as well as the increase of aggregated $Aβ_{1-42}$ concentration (Figure S4C). The cell viability was found to be decreased to 42 ± 7% after the neurons were stimulated by 60 μM aggregated $Aβ_{1-42}$ for 48 h. When the concentration of aggregated $Aβ_{1-42}$ was increased to 100 μM, the cell viability was decreased down to 21 ± 4% after the neurons were stimulated for 48 h. This result indicated that the aggregated $Aβ_{1-42}$ had close relationship with the neuronal death. Autophagy has been considered to contribute to cell death (Yang et al., 2017; Kroemer and Jäättelä, 2005; Yang and Klionsky, 2010); therefore, the level of autophagy after the neurons were stimulated by aggregated $Aβ_{1-42}$ was also investigated. As shown in Figure 6A, the fluorescence of the neurons incubated with MDC gradually decreased after the neurons were stimulated by 60 μM aggregated $Aβ_{1-42}$ from 0 to 48 h. Meanwhile, the amount of LC3-II gradually decreased after the neurons were stimulated by $Aβ_{1-42}$ from 0 to 48 h (Figure 6B). The intensity ratio of LC3-II to β-actin changed from 1.10 ± 0.08 to 0.74 ± 0.05 after the neurons were stimulated by $Aβ_{1-42}$ for 48 h, indicating the level of autophagy was gradually decreased after the neurons were stimulated by 60 μM aggregated $Aβ_{1-42}$ from 0 to 48 h. Notably, seldom decrease (0.03 ± 0.01) of LC3-II was observed after neurons were stimulated by $Aβ_{1-42}$ for 48 h in the presence of VeRa, demonstrating that VaRa can prevent Aβ-induced decreasing of autophagy (Figure 6C). Previous studies have reported that autolysosomes were produced by fusion of lysosomes and autophagosomes, which contributed to autophagy level. For understanding the molecular mechanism of $Aβ_{1-42}$-induced autophagy, we explored the changes of lysosomal pH and Ca^{2+} in neurons during $Aβ_{1-42}$ stimulation. With the extension of stimulation time from 0 to 48 h during 60 μM $Aβ_{1-42}$ stimulation, pH_{ly} was continuously increased from 4.83 ± 0.05 to 6.90 ± 0.30, whereas $[Ca^{2+}]_{ly}$ was decreased from 525 ± 20 to 15 ± 1 μM. More importantly, addition of Vera can apparently inhibit the increase in pH_{ly} (5.43 ± 0.27) and the decrease in $[Ca^{2+}]_{ly}$ (447 ± 23 μM) (Figures 6D–6J and S4D). Since normal pH value and Ca^{2+} concentration are essential for lysosomal functions, these significant changes in lysosomal pH and Ca^{2+} concentration would lead to lysosomal dysfunction, further reduce autophagy level by inhibiting the fusion of lysosomes and autophagosomes. Consequently, Aβ-induced neuronal death was attributed to Aβ-caused lysosomal dysfunction by greatly improving lysosomal pH and significantly reducing lysosomal Ca^{2+} concentration, which give rise to the autophagy abnormal, thus resulting in neuronal death (Figure 6K).

Activation of Quiescent Neural Stem Cell for Antiaging by Regulating Autophagy

Neural stem cells (NSCs) are a typical type of cells in the nervous system, which can produce newborn neurons during the process of neurogenesis. Generally, NSCs can be divided into quiescent NSCs (qNSCs) and active NSCs (aNSCs) (Figures S5A–S5F). More interestingly, qNSCs can be activated and transformed into aNSCs, and this process was regulated by lysosomal activity and the level of autophagy (Leeman et al., 2018). Meanwhile, we have found that lysosomal activity and autophagy levels can be regulated by lysosome pH and Ca^{2+} concentration. Thus, in order to understand the molecular mechanism regulating the activation ability of qNSCs, pH value and Ca^{2+} concentration of qNSCs and aNSCs in lysosomes and the degree of autophagy were first measured. As shown in Figures 7A and 7B, lysosomal pH in qNSCs was estimated to 4.98 ± 0.16, slightly higher than that in aNSCs (4.70 ± 0.12). However, lysosomal Ca^{2+} concentration in qNSCs (465 ± 25 μM) was obviously lower than that in aNSCs (575 ± 20 μM). At the same time, we observed that LC3-II/β-actin was about 0.47 ± 0.07 in qNSCs by western blot and the degree of autophagy was lower than that of aNSCs (LC3-II/β-actin = 1.10 ± 0.04) (Figures 7J and 7K). Therefore, the level of autophagy in aNSCs is higher than that in qNSCs. Since qNSCs can be activated and transformed into aNSCs under simultaneous stimulation of epidermal growth factor (EGF) and

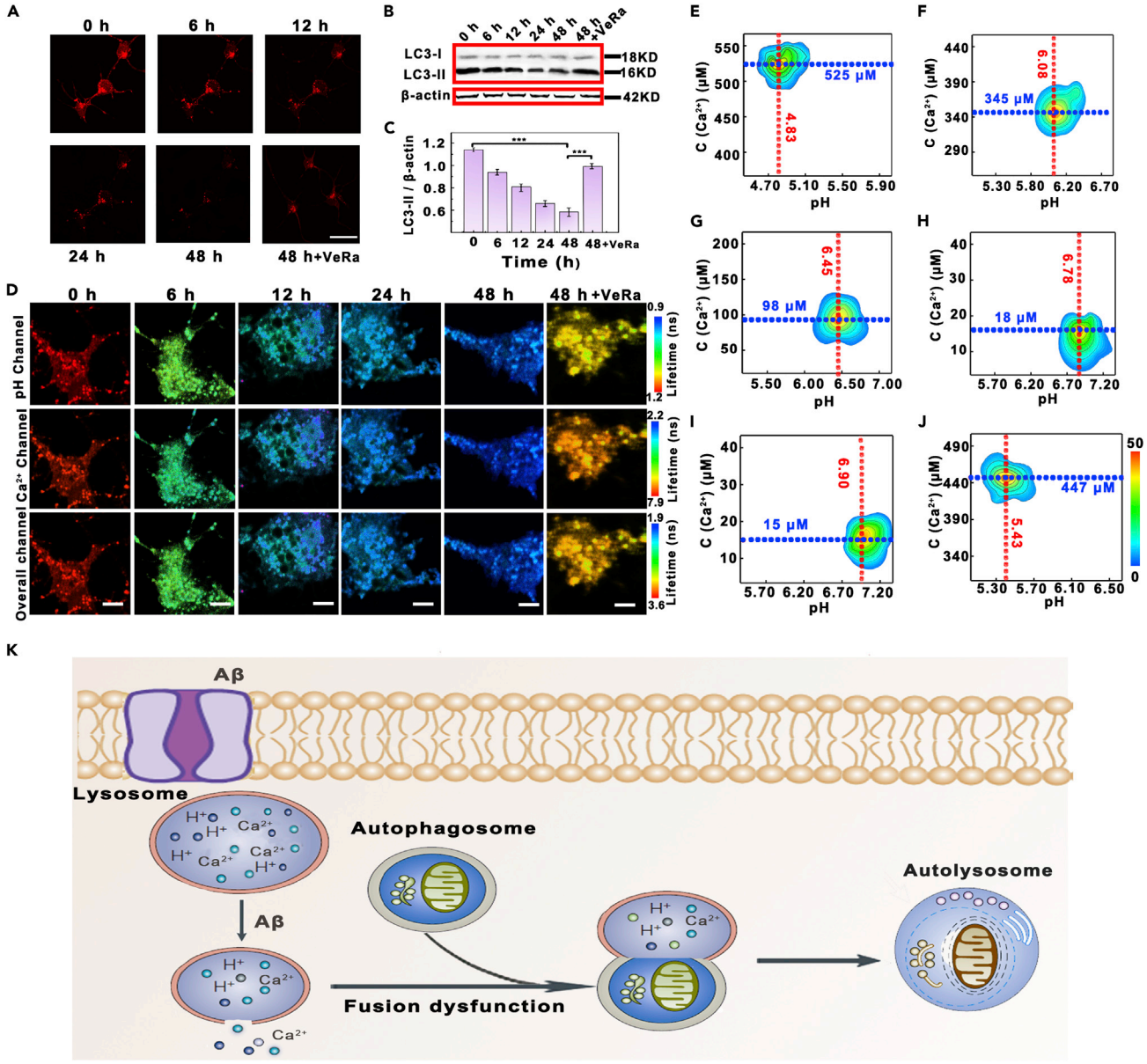

Figure 6. Fluorescence Lifetime Imaging and Quantification of Lysosomal Ca^{2+} and pH in Neurons under Stimulation of Aggregated $A\beta_{1-42}$

(A) Fluorescence images of neurons incubated with MDC after the neurons were stimulated by aggregated $A\beta_{1-42}$ for different times (0, 6, 12, 24, 48 h and 48 h in the presence of VeRa). Scale bar: 25 μm.

(B) Immunoblotting analysis of relative levels of LC3-I and LC3-II in lysate purified from the neurons that were incubated with 60 μM Aβ for different times (0, 6,12, 24, and 48 h) and 60 μM Aβ for 48 h in the presence of VeRa.

(C) The quantification of LC3-II/β-actin expression from western blot results. Data are expressed as mean ± SD of five samples in each experimental group. Assume that the significance level of the statistical test is 0.001 (***) (n = 20; ***, $p < 0.001$).

(D) Enlarged confocal fluorescence lifetime images of neurons collected from pH channel, Ca^{2+} channel, and overall channels after neurons were stimulated with 60 μM aggregated $A\beta_{1-42}$ for different times (0, 6, 12, 24, and 48 h) and 60 μM aggregated $A\beta_{1-42}$ for 48 h in the presence of VeRa. Scale bar: 8 μm.

(E–J) Lysosomal density scatter profiles of neurons after incubation with Aβ for (E) 0, (F) 6, (G) 12, (H) 24, (I) 48 hr and (J) 48 hr in the presence of VeRa. The density plot was pseudo color, red and blue correspond to populations with higher and lower frequencies of occurrence. The data were obtained from 100 lysosomes in 10 cells.

(K) Schematic of lysosomal pH and Ca^{2+}-mediated regulation of autophagy.

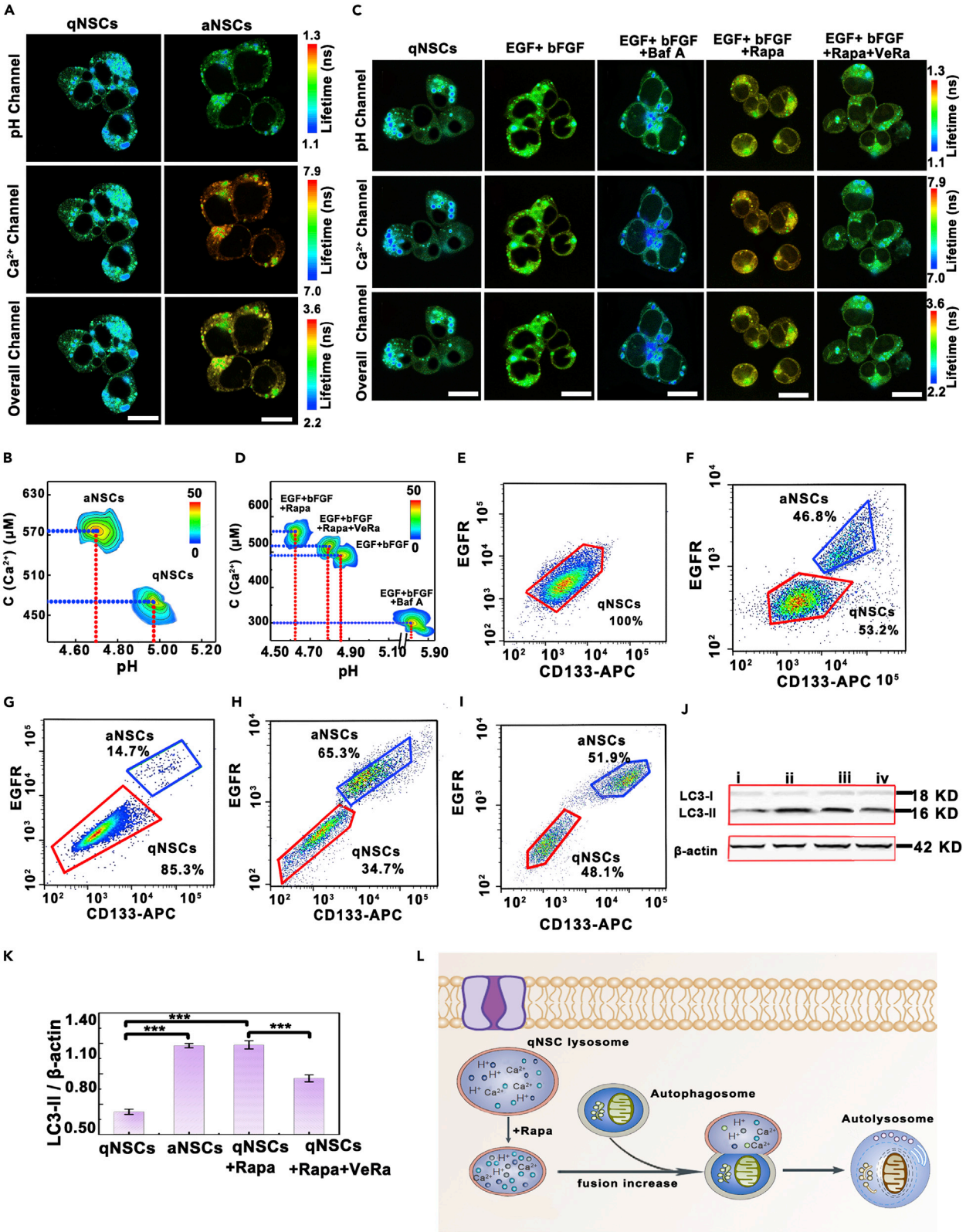
A
qNSCs
aNSCs
pH Channel
Ca2+ Channel
Overall Channel
1.3
1.1
Lifetime (ns)
7.9
7.0
3.6
2.2
C
qNSCs
EGF+ bFGF
EGF+ bFGF +Baf A
EGF+ bFGF +Rapa
EGF+ bFGF +Rapa+VeRa
B
aNSCs
qNSCs
C (Ca2+) (μM)
pH
D
EGF+bFGF +Rapa
EGF+bFGF +Rapa+VeRa
EGF+bFGF
EGF+bFGF +Baf A
E
EGFR
CD133-APC
qNSCs 100%
F
aNSCs 46.8%
qNSCs 53.2%
CD133-APC 10^5
G
aNSCs 14.7%
qNSCs 85.3%
H
aNSCs 65.3%
qNSCs 34.7%
I
aNSCs 51.9%
qNSCs 48.1%
J
i
ii
iii
iv
LC3-I
LC3-II
18 KD
16 KD
β-actin
42 KD
K
LC3-II / β-actin
***
qNSCs
aNSCs
qNSCs +Rapa
qNSCs +Rapa+VeRa
L
qNSC lysosome
Autophagosome
+Rapa
fusion increase
Autolysosome

Figure 7. Fluorescence Lifetime Imaging and Quantification of Lysosomal Ca^{2+} and pH in qNSCs and aNSCs

(A) Confocal fluorescence lifetime images of qNSCs and aNSCs collected from pH channel, Ca^{2+} channel, and overall channel. Scale bar: 10 μm.

(B) Lysosomal density scatter profiles of neural stem cells. The density plot was pseudo color, red and blue correspond to populations with higher and lower frequencies of occurrence. The data were obtained from 100 lysosomes in 10 cells.

(C) Confocal fluorescence lifetime images of qNSCs stimulated with EGF and bFGF. For comparison, the image of qNCSs stimulated by EGF and bFGF in the presence of bafilomycin A_1 (Baf A), rapamycin (Rapa), and Rapa and VeRa was also obtained. Scale bar: 10 μm.

(D) Lysosomal density scatter profiles of qNSCs stimulated by bafilomycin A_1, rapamycin, and rapamycin and VeRa. The density plot was pseudo color, here red and blue correspond to populations with higher and lower frequencies of occurrence. The data were obtained from 100 lysosomes in 10 cells.

(E–I) FACS sorting scheme used to isolate qNSCs and aNSCs. (E) qNCSs, (F) qNSCs and aNSCs after qNSCs were stimulated with EGF and bFGF, (G) EGF and bFGF in the presence of bafilomycin A_1, (H) EGF and bFGF in the presence of rapamycin, (I) EGF and bFGF in the presence of rapamycin and VeRa.

(J) Immunoblotting analysis of relative levels of LC3-I, LC3-II in lysate purified from (i) qNSCs, (ii) aNSCs, (iii) qNSCs stimulated by Rapa, and (**iv**) qNSCs stimulated by Rapa in the presence of VeRa.

(K) The quantification of LC3-II/β-actin expression on western blot. Data are expressed as mean ± SD of five samples in each experimental group. Assume that the significance level of the statistical test is 0.001 (***) (n = 20; ***, $p < 0.001$).

(L) Schematic of rapamycin as an anti-aging agent.

basic fibroblast growth factor (bFGF), the changes in the levels of autophagy as well as in lysosomal pH value and Ca^{2+} concentration in qNSCs under the stimulation of EGF and bFGF were further investigated. As shown in Figures 7C and 7D, lysosomal pH value and Ca^{2+} concentration in qNSCs were estimated to be 4.98 ± 0.16 and 465 ± 25 μM, respectively. However, after qNSCs were stimulated by EGF and bFGF for 2 days, lysosomal pH value and Ca^{2+} concentration in qNCSs changed to 4.86 ± 0.38 and 523 ± 47 μM, which were similar to those obtained in aNSCs. Furthermore, from the western bolt results, we found that the level of autophagy (LC3-II/β-actin = 1.03 ± 0.02) in qNCSs rose and approached the level of autophagy in aNSCs (LC3-II/β-actin = 1.18 ± 0.05) upon stimulation, indicating the level of autophagy was also increased. In addition, FACS results implied that 46.8 ± 2.5% of qNSCs were transformed into aNSCs after qNSCs were stimulated by EGF and bFGF for 2 days (n = 5) (Figures 7E and 7F). More interestingly, after qNCSs were stimulated by EGF and bFGF in the presence of VeRa for 2 days, seldom change was observed for lysosomal pH (4.92 ± 0.18) and Ca^{2+} concentration (480 ± 32 μM) in qNCSs, which were similar to those obtained in qNSCs (Figures S5G and S5H). Moreover, no obvious change was obtained in autophagy levels (LC3-II/β-actin = 0.54), indicating that the prevention of changes in $[Ca^{2+}]_{ly}$ can inhibit the change of autophagy level. Furthermore, FACS results implied that 23.2 ± 2.9% of qNSCs were transformed into aNSCs after stimulation by EGF and bFGF in the presence of VeRa for 2 days (n = 5) (Figure S5I). These results demonstrated that $[Ca^{2+}]_{ly}$ changes had an obvious effect on lysosomal pH and the level of autophagy and further influences the activation of qNCSs.

On the other hand, we observed the activation ability of qNSCs by changing lysosomal pH. We found that, after the pH value of qNSCs was adjusted to 4.00, 35.8 ± 2.7% qNSCs (n = 5) were transformed into aNSCs. When lysosomal pH was increased to 4.45, the transformation ability of qNSCs into aNSCs showed the highest value of 50.1 ± 2.4%. More interestingly, after the lysosomal pH gradually increased from 4.45 to 6.00, the transformation ratio was decreased instead. When pH value was controlled to 6.00, the ability of qNSCs transferred into aNSCs was decreased down to 8.7 ± 0.5% (Figures S6A–S6I). Therefore, the activation ability of qNSCs transferred into aNSCs demonstrated the highest value at the optimized lysosomal pH of 4.45. Moreover, it was found that the degree of autophagy was also the highest (LC3-II/β-actin = 1.87 ± 0.06) at this pH value. When lysosome pH changed from 4.45 to 4.00 or 4.45 to 6.00, the autophagic level was significantly decreased (Figures S6J and S6K). These results demonstrated that lysosomal pH was significantly important to regulate the level of autophagy and then to affect the activation ability of qNSCs. Then, the results were further confirmed by addition of bafilomycin A_1, which significantly prevented the decrease of pH_{ly} and increase of $[Ca^{2+}]_{ly}$ in qNSCs. In addition, the level of autophagy in qNSCs was remarkably reduced (LC3-II/β-actin = 0.4). Only 14.7 ± 2.8% qNSCs were transformed into aNSCs (n = 5) (Figures 7E and 7G). These results strongly suggested that the regulation of lysosomal pH (0.5 pH) and Ca^{2+} concentration (580 ± 27 μM) is possibly to promote lysosomal activity, increase autophagy, and further regulate lysosomal-mediated qNSCs activation capacity.

It has been reported that aging has a close relationship with lysosomal activity, the ability of qNSCs activation, and the number of aNSCs. More importantly, although previous study has proved rapamycin (Rapa), an anti-aging drug, has the ability of antiaging, the actual molecular mechanism of rapamycin-induced antiaging is still unclear (Laraia et al., 2019; Leeman et al., 2018; Rubinsztein et al., 2011). For this purpose, we next investigated the function of lysosome during rapamycin-induced antiaging. As shown in Figures 7C and 7H, after qNSCs were stimulated by EGF and bFGF in the presence of 10 nM Rapa for 2 days, 65.3 ± 6.0% qNSCs were transformed into aNSCs. At the same time, lysosomal pH was decreased to 4.62 ± 0.20, whereas lysosomal Ca^{2+}

concentration was increased to 570 ± 28 μM (Figure 7D). Moreover, it was found that autophagy was enhanced by stimulation of qNSCs with EGF and bFGF in the presence of 10 nM Rapa (LC3-II/β-actin = 1.10 ± 0.04), proving Rapa contributed to the activity of lysosomes and the level of autophagy. To our surprise, after addition of VeRa, seldom decrease in pH_{ly} (4.80 ± 0.15) and no apparent increase in $[Ca^{2+}]_{ly}$ (508 ± 23 μM) were observed. The results suggested that the level of autophagy was decreased after the addition of Vera (LC3-II/β-actin = 0.82 ± 0.01) and the ability of qNSCs transferred to aNSCs was also decreased to 51.9 ± 3.5% (n = 5) (Figures 7D and 7I), further indicating that inhibiting the change of the concentration of lysosomal Ca^{2+} can reduce the effect of Rapa. The data implied that rapamycin-induced antiaging can be regulated through promoting lysosomal activity. Since lysosomal activity is closely related to autophagy, we can conclude that the antiaging ability of rapamycin was realized by increasing autophagy level through regulating lysosomal pH and Ca^{2+} concentration (Figure 6L).

Meanwhile, the mathematical model for correlation among the concentration of Ca^{2+}, pH value, and bio-processes (aging and ant-aging) was also constructed. In this work, the transformation rate of qNSCs to aNCSs (denoted as α) over 45% was defined as "antiaging," whereas $\alpha \leq 45\%$ was defined as "aging." As shown in Figure S6L, when α changed from 45.0% to 50.1%, the lysosomal pH increased from 4.45 to 4.75, whereas the concentration of Ca^{2+} decreased from 580 to 480 μM. Thus, the composed area was defined as antiaging, recorded as "Zone 1." On the other hand, when α decreased from 45.0% to 19.7%, the lysosomal pH varied in the range of 4.50–5.50, whereas the concentration of Ca^{2+} changed from 400 to 600 μM. The composed area (except for "Zone 1") is defined as "aging," and it is recorded as "Zone 0." When the lysosomal pH was higher than 5.50 or lower than 4.45, as well as Ca^{2+} concentration was higher than 600 μM or lower than 400 μM, the cell was in an abnormal state. These findings provide new insights into the regulation of aging caused by decreased activation of neural stem cells.

DISCUSSION

A single DNA-based FLIM reporter was developed for exploring the roles of lysosomal pH and Ca^{2+} in regulating autophagy, in which a new FLIM Ca^{2+} probe was designed and assembled onto a DNA nanostructure together with pH-responsive and lysosome-targeted molecules. The DNA nanostructure with precisely controllable size and shape enabled simultaneous determination of pH and Ca^{2+} at the same localization without FRET or cross talk. In addition, taking the advantages of FLIM, the developed nanoprobe showed high accuracy with high spatial resolution. More importantly, the assembled DNA reporter showed long-term structural stability, which was very beneficial for real-time imaging and biosensing of pH and Ca^{2+} in lysosomes.

Using this useful and powerful tool, it was found that lysosomal pH increased with decreasing concentration of Ca^{2+}, whereas the concentration of Ca^{2+} went down with rising pH value. Both pH value and concentration of Ca^{2+} in lysosomes was discovered to regulate the autophagy. Furthermore, the experimental results suggested that Aβ-induced neuronal death resulted from autophagy abnormal, which was regulated by improving lysosomal pH and reducing Ca^{2+} concentration. Moreover, it was found that the transformation of qNSCs to aNSCs was regulated by autophagy and Rapa-induced antiaging was realized by improving the level autophagy through regulating lysosomal pH and Ca^{2+} concentration.

This work has systematically studied the roles of lysosomal pH and Ca^{2+} to regulate the autophagy, which gives a new insight into understanding autophagy-related processes such as neurodegenerative diseases and aging. More importantly, this study has provided a new methodology for real-time tracking and simultaneous determination of multiple substances in cells, even in organelles, based on stable DNA nanostructures with different shapes such as octahedron and cylindrical.

Limitations of the Study

The signal collection time of FLIM imaging method is longer than that of the fluorescence intensity-based imaging method. Therefore, it is necessary to develop an ultrafast imaging method in the future studies.

Resource Availability

Lead Contact

Further information and requests for resources and reagents should be directed to and will be fulfilled by the Lead Contact, Yang Tian (ytian@chem.ecnu.edu.cn)

Materials Availability

All the materials necessary to reproduce this study are included in the manuscript and Supplemental Information.

Data and Code Availability

The data that support the findings of this study are available from the corresponding author upon reasonable request.

METHODS

All methods can be found in the accompanying Transparent Methods supplemental file.

SUPPLEMENTAL INFORMATION

Supplemental Information can be found online at https://doi.org/10.1016/j.isci.2020.101344.

ACKNOWLEDGMENT

The authors greatly appreciate the financial support from NSFC (21635003 and 21811540027). This work also was supported by Innovation Program of Shanghai Municipal Education Commission (201701070005E00020) and the China Postdoctoral Science Foundation (2019TQ0095).

AUTHOR CONTRIBUTIONS

Y.T. designed the experiments, wrote the manuscript, and was responsible for the work. Z.L. and Z.Z. performed the experiments and wrote the manuscript. All the authors discussed the results and commented on the manuscript.

DECLARATION OF INTERESTS

The authors declare no competing interests.

Received: January 27, 2020
Revised: April 24, 2020
Accepted: July 1, 2020
Published: July 24, 2020

REFERENCES

Bagh, M.B., Peng, S., Chandra, G., Zhang, Z., Singh, S.P., Pattabiraman, N., Liu, A., and Mukherjee, A.B. (2017). Misrouting of v-ATPase subunit V0a1 dysregulates lysosomal acidification in a neurodegenerative lysosomal storage disease model. Nat. Commun. *8*, 14612.

Biederbick, A., Kern, H.F., and Elsässer, H.P. (1995). Monodansylcadaverine (MDC) is a specific in vivo marker for autophagic vacuoles. Eur. J. Cell Biol. *66*, 3–14.

Christensen, K.A., Myers, J.T., and Swanson, J.A. (2002). pH-dependent regulation of lysosomal calcium in macropHages. J. Cell. Sci. *115*, 599–607.

Chung, C.Y.-S., Shin, H.R., Berdan, C.A., Ford, B., Ward, C.C., Olzmann, J.A., Zoncu, R., and Nomura, D.K. (2019). Covalent targeting of the vacuolar H^+-ATPase activates autophagy via mTORC1 inhibition. Nat. Chem. Biol. *15*, 776–785.

Cui, Z., Zhang, Y., Xia, K., Yan, Q., Kong, H., Zhang, J., Zuo, X., Shi, J., Wang, L., Zhu, Y., et al. (2018). Nanodiamond autophagy inhibitor allosterically improves the arsenical-based therapy of solid tumors. Nat. Commun. *9*, 4347.

Dong, B., Song, X., Wang, C., Kong, X., Tang, Y., and Lin, W. (2016). Dual site-controlled and lysosome-targeted intramolecular charge transfer-photoinduced electron transfer-fluorescence resonance energy transfer fluorescent probe for monitoring pH changes in living cells. Anal. Chem. *88*, 4085–4091.

Egawa, T., Hanaoka, K., Koide, Y., Ujita, S., Takahashi, N., Ikegaya, Y., Matsuki, N., Terai, T., Ueno, T., Komatsu, T., et al. (2011). Development of a far-red to near-infrared fluorescence probe for calcium ion and its application to multicolor neuronal imaging. J. Am. Chem. Soc. *133*, 14157–14159.

Erben, C.M., Goodman, R.P., and Turberfield, A.J. (2007). A self-assembled DNA bipyramid. J. Am. Chem. Soc. *129*, 6992–6993.

Fan, Y., Wang, P., Lu, Y., Wang, R., Zhou, L., Zheng, X., Li, X., Piper, J.A., and Zhang, F. (2018). Lifetime-engineered NIR-II nanoparticles unlock multiplexed in vivo imaging. Nat. Nanotech. *13*, 941–946.

Green, E.M., Barrett, C.F., Bultynck, G., Shamah, S.M., and Dolmetsch, R.E. (2007). The tumor suppressor eIF3e mediates calcium-dependent internalization of the L-type calcium channel CaV1.2. Neuron *55*, 615–632.

Jiang, K., Sun, S., Zhang, L., Lu, Y., Wu, A., Cai, C., and Lin, H. (2015). Red, green, and blue luminescence by carbon dots: full-color emission tuning and multicolor cellular imaging. Angew. Chem. Int. Ed. *54*, 5360–5363.

Kawai, K., Osakada, Y., Takada, T., Fujitsuka, M., and Majima, T. (2004). Lifetime regulation of the charge-separated state in DNA by modulating the oxidation potential of guanine in DNA through hydrogen bonding. J. Am. Chem. Soc. *126*, 12843–12846.

Khurana, V., Elson-Schwab, I., Fulga, T.A., Sharp, K.A., Loewen, C.A., Mulkearns, E., Tyynelä, J., Scherzer, C.R., and Feany, M.B. (2010). Lysosomal dysfunction promotes cleavage and neurotoxicity of Tau in vivo. PLoS Genet. *6*, e1001026.

Komatsu, M., Waguri, S., Chiba, T., Murata, S., Iwata, J.-I., Tanida, I., Ueno, T., Koike, M., Uchiyama, Y., Kominami, E., et al. (2006). Loss of autophagy in the central nervous system causes neurodegeneration in mice. Nature *441*, 880–884.

Kong, B., Zhu, A., Luo, Y., Tian, Y., Yu, Y., and Shi, G. (2011). Sensitive and selective colorimetric visualization of cerebral dopamine based on double molecular recognition. Angew. Chem. Int. Ed. *50*, 1837–1840.

Kong, B., Zhu, A., Ding, C., Zhao, X., Li, B., and Tian, Y. (2012). Carbon dot-based inorganic-organic nanosystem for two-photon imaging and biosensing of pH variation in living cells and tissues. Adv. Mater. *24*, 5844–5848.

Kroemer, G., and Jäättelä, M. (2005). Lysosomes and autophagy in cell death control. Nat. Rev. Cancer *5*, 886–897.

Kwon, Y.-H., and Triggle, D.J. (1991). Chiral aspects of drug action at ion channels: a commentary on the stereoselectivity of drug actions at voltage-gated ion channels with particular reference to verapamil actions at the Ca^{2+} channel. Ehirality *3*, 393–404.

Laraia, L., Friese, A., Corkery, D.P., Konstantinidis, G., Erwin, N., Hofer, W., Karatas, H., Klewer, L., Brockmeyer, A., Metz, M., et al. (2019). The cholesterol transfer protein GRAMD1A regulates autophagosome biogenesis. Nat. Chem. Biol. *15*, 710–720.

Leeman, D.S., Hebestreit, K., Ruetz, T., Webb, A.E., McKay, A., Pollina, E.A., Dulken, B.W., Zhao, X., Yeo, R.W., Ho, T.T., et al. (2018). Lysosome activation clears aggregates and enhances quiescent neural stem cell activation during aging. Science *359*, 1277–1282.

Li, Y., Wang, Y., Yang, S., Zhao, Y., Yuan, L., Zheng, J., and Yang, R. (2015). Hemicyanine-based high resolution ratiometric near-infrared fluorescent probe for monitoring pH changes in vivo. Anal. Chem. *87*, 2495–2503.

Li, W., Fang, B., Jin, M., and Tian, Y. (2017a). Two-photon ratiometric fluorescence probe with enhanced absorption cross section for imaging and biosensing of zinc ions in hippocampal tissue and zebrafish. Anal. Chem. *89*, 2553–2560.

Li, J., Green, A.A., Yan, H., and Fan, C. (2017b). Engineering nucleic acid structures for programmable molecular circuitry and intracellular biocomputation. Nat. Chem. *9*, 1056–1067.

Li, J., Zhu, R., Chen, K., Zheng, H., Zhao, H., Yuan, C., Zhang, H., Wang, C., and Zhang, M. (2018). Potent and specific Atg8-targeting autophagy inhibitory peptides from giant ankyrins. Nat. Chem. Biol. *14*, 778–787.

Lin, M., Song, P., Zhou, G., Zuo, X., Aldalbahi, A., Lou, X., Shi, J., and Fan, C. (2016). Electrochemical detection of nucleic acids, proteins, small molecules and cells using a DNA-nanostructure-based universal biosensing platform. Nat. Protoc. *11*, 1244–1263.

Liu, W., Dong, H., Zhang, L., and Tian, Y. (2017). Development of an efficient biosensor for the in vivo monitoring of Cu^{+} and pH in the brain: rational design and synthesis of recognition molecules. Angew. Chem. Int. Ed. *56*, 16328–16332.

Liu, Z., Pei, H., Zhang, L., and Tian, Y. (2018a). Mitochondria-targeted DNA nanoprobe for real-time imaging and simultaneous quantification of Ca^{2+} and pH in neurons. ACS Nano *12*, 12357–12368.

Liu, Z., Wang, S., Li, W., and Tian, Y. (2018b). Bioimaging and biosensing of Ferrous ion in neurons and HepG2 cells upon oxidative stress. Anal. Chem. *90*, 2816–2825.

Liu, Z., Jing, X., Zhang, S., and Tian, Y. (2019a). A copper nanocluster-based fluorescent probe for real-time imaging and ratiometric biosensing of calcium ions in neurons. Anal. Chem. *91*, 2488–2497.

Liu, Z., Wu, P., Yin, Y., and Tian, Y. (2019b). A ratiometric fluorescent DNA nanoprobe for cerebral adenosine triphosphate assay. Chem. Commun. (Camb.) *55*, 9955–9958.

Luzio, J.P., Pryor, P.R., and Bright, N.A. (2007). Lysosomes: fusion and function. Nat. Rev. Mol. Cell. Biol. *8*, 622–632.

Minamiki, T., Sekine, T., Aiko, M., Su, S., and Minami, T. (2019). An organic FET with an aluminum oxide extended gate for pH sensing. Sens. Mater. *31*, 99–106.

Narayanaswamy, N., Chakraborty, K., Saminathan, A., Zeichner, E., Leung, K., and Krishnan, Y. (2019). A pH-correctable, DNA-based fluorescent reporter for organellar calcium. Nat. Methods *16*, 95–102.

Omen, P., Aref, M.A., Kaya, I., Phan, N.T.N., and Ewing, A.G. (2019). Chemical analysis of single cells. Anal. Chem. *91*, 588–621.

Pan, W., Wang, H., Yang, L., Yu, Z., Li, N., and Tang, B. (2016). Ratiometric Fluorescence nanoprobes for subcellular pH imaging with a single-wavelength excitation in living cells. Anal. Chem. *88*, 6743–6748.

Rampe, D., and Triggle, D.J. (1990). New ligands for L-type Ca^{2+} channels. Trends Pharmacol. Sci. *11*, 112–115.

Rubinsztein, D.C., Mariño, G., and Kroemer, G. (2011). Autophagy and aging. Cell *146*, 682–695.

Sakamoto, M., Cai, X., Hara, M., Tojo, S., Fujitsuka, M., and Majima, T. (2005). Anomalous fluorescence from the azaxanthone ketyl radical in the excited state. J. Am. Chem. Soc. *127*, 3702–3703.

Settembre, C., Fraldi, A., Medina, D.L., and Ballabio, A. (2013). Signals from the lysosome: a control center for cellular clearance and energy metabolism. Nat. Rev. Mol. Cell. Biol. *14*, 283–296.

Shcherbakova, D.M., Cammer, N.C., Huisman, T.M., Verkhusha, V.V., and Hodgson, L. (2018). Direct multiplex imaging and optogenetics of Rho GTPases enabled by near-infrared FRET. Nat. Chem. Biol. *14*, 591–600.

Shen, D., Wang, X., Li, X., Zhang, X., Yao, Z., Dibble, S., Dong, X., Yu, T., Lieberman, A.P., Showalter, H.D., and Xu, H. (2012). Lipid storage disorders block lysosomal trafficking by inhibiting a TRP channel and lysosomal calcium release. Nat. Commun. *3*, 731.

Shen, S.-L., Chen, X.-P., Zhang, X.-F., Miao, J.-Y., and Zhao, B.-X. (2015). A rhodamine B-based lysosomal pH probe. J. Mater. Chem. B *3*, 919–925.

Song, S., Qin, Y., He, Y., Huang, Q., Fan, C., and Chen, H.-Y. (2010). Functional nanoprobes for ultrasensitive detection of biomolecules. Chem. Soc. Rev. *39*, 4234–4243.

Tachikawa, T., Fujitsuka, M., and Majima, T. (2007). Mechanistic insight into the TiO_2 photocatalytic reactions: design of new photocatalysts. J. Phys. Chem. C *111*, 5259–5275.

Tang, B., Yu, F., Li, P., Tong, L., Duan, X., Xie, T., and Wang, X. (2009). A near-infrared neutral pH fluorescent probe for monitoring minor pH changes: imaging in living HepG2 and HL-7702 cells. J. Am. Chem. Soc. *131*, 3016–3023.

Tian, T., Sun, Y., Wu, H., Pei, J., Zhang, J., Zhang, Y., Wang, L., Li, B., Wang, L., Shi, J., et al. (2016). Acupuncture promotes mTOR-independent autophagic clearance of aggregation-prone proteins in mouse brain. Sci. Rep. *6*, 19714.

Wan, Q., Chen, S., Shi, W., Li, L., and Ma, H. (2014). Lysosomal pH rise during heat shock monitored by a lysosome-targeting near-infrared ratiometric fluorescent probe. Angew. Chem. Int. Ed. *53*, 10916–10920.

Wang, W., Zhao, F., Li, M., Zhang, C., Shao, Y., and Tian, Y. (2019a). A SERS optophysiological probe for the real-time mapping and simultaneous determination of the carbonate concentration and pH value in a live mouse brain. Angew. Chem. Int. Ed. *58*, 5256–5260.

Wang, H., Yao, H., Li, C., Shi, H., Lan, J., Li, Z., Zhang, Y., Liang, L., Fang, J.-Y., and Xu, J. (2019b). HIP1R targets PD-L1 to lysosomal degradation to alter T cell–mediated cytotoxicity. Nat. Chem. Biol. *15*, 42–50.

Yang, Z., and Klionsky, D.J. (2010). Eaten alive: a history of macroautophagy. Nat. Cell. Biol. *12*, 814–822.

Yang, L., Chen, Y., Yu, Z., Pan, W., Wang, H., Li, N., and Tang, B. (2017). Dual-ratiometric fluorescent nanoprobe for visualizing the dynamic process of pH and superoxide anion changes in autophagy and apoptosis. ACS Appl. Mater. Interface *9*, 27512–27521.

Zhang, P., Beck, T., and Tan, W. (2001). Design of a molecular beacon DNA probe with two fluorophores. Angew. Chem. Int. Ed. *40*, 402–405.

Zhu, A., Qu, Q., Shao, X., Kong, B., and Tian, Y. (2012). Carbon-dot-based dual-emission nanohybrid produces a ratiometric fluorescent sensor for in vivo imaging of cellular copper ions. Angew. Chem. Int. Ed. *51*, 7185–7189.

Zhu, M.X., Tuo, B., and Yang, J.J. (2016). The hills and valleys of calcium signaling. Sci. China. Life Sci. *59*, 743–748.

iScience, Volume *23*

Supplemental Information

A DNA-Based FLIM Reporter for Simultaneous Quantification of Lysosomal pH and Ca^{2+} during Autophagy Regulation

Zhonghui Zhang, Zhichao Liu, and Yang Tian

Supplemental Information

Supplemental Figures and Legends

Table S1. Oligonucleotides used in this work purchased from Takara Bio Company. Related to Figure 1.

Name	Sequences (5' to 3')	5' Label	Purification
a	CGAACATTCCTAAGTCTGAAATTTATCACCCG CCATAGTAGACGTATCACCAGGCAGTTGAGA	MP	HPLC
b	CTTGCTACACGATTCAGACTTAGGAATGTTCG ACATGCGAGGGTCCAATACCGACGATTACAG		HPLC
c	CGTGTAGCAAGCTGTAATCGACGGGAAGAGC ATGCCCATCCACTACTATGGCGGGTGATAAAA	CHO	HPLC
A	TCTAGTCTCTACGTCAAGTAAGAACCTTAGCT GCGCGGATGACTCAACTGCCTGGTGATACGA	MP	HPLC
B	CGGTATTGGACCCTCGCATGACATCCGCGCAG CTAAGGTTCAAAGTTCCTGCCGCTTCACGGA	MP	HPLC
C	TACTTGACGTAGAGACTAGAAGGATGGGCATG CTCTTCCCGACCGTGAAGCGGCAGGAACTTA	RhB	HPLC
C1	TACTTGACGTAGAGACTAGAAGGATGGGCATG CTCTTCCCGACCGTGAAGCGGCAGGAACTTA	CHO	HPLC

Table S2. T-test results of pH sensing by using DND-189 probe and our developed nanoprobe (α = 0.05, f= 4). Related to Figure 3.

pH	DND-189	Mean±SD (n=3)	Our nanoprobe	Mean±SD (n=3)	t ($t_{\alpha, f}$)
3.00	2.99, 3.01, 3.05	3.01±0.06	3.02, 3.06, 2.92	3.00±0.05	0.22 (2.78)
4.00	4.04, 3.95, 3.98	3.99±0.01	4.05, 3.96, 3.95	3.98±0.03	0.24 (2.78)

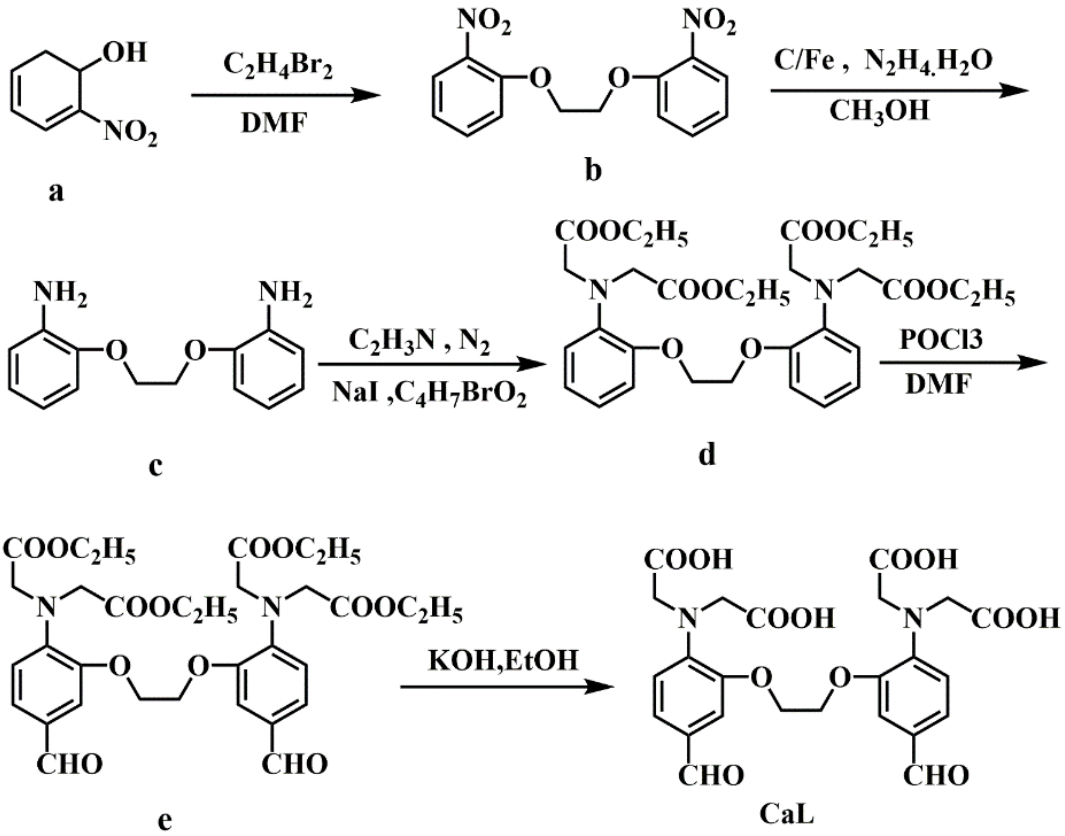

Scheme S1. Synthesis of Ca^{2+} ion ligand (CaL) with two aldehyde groups. Related to Figure 1.

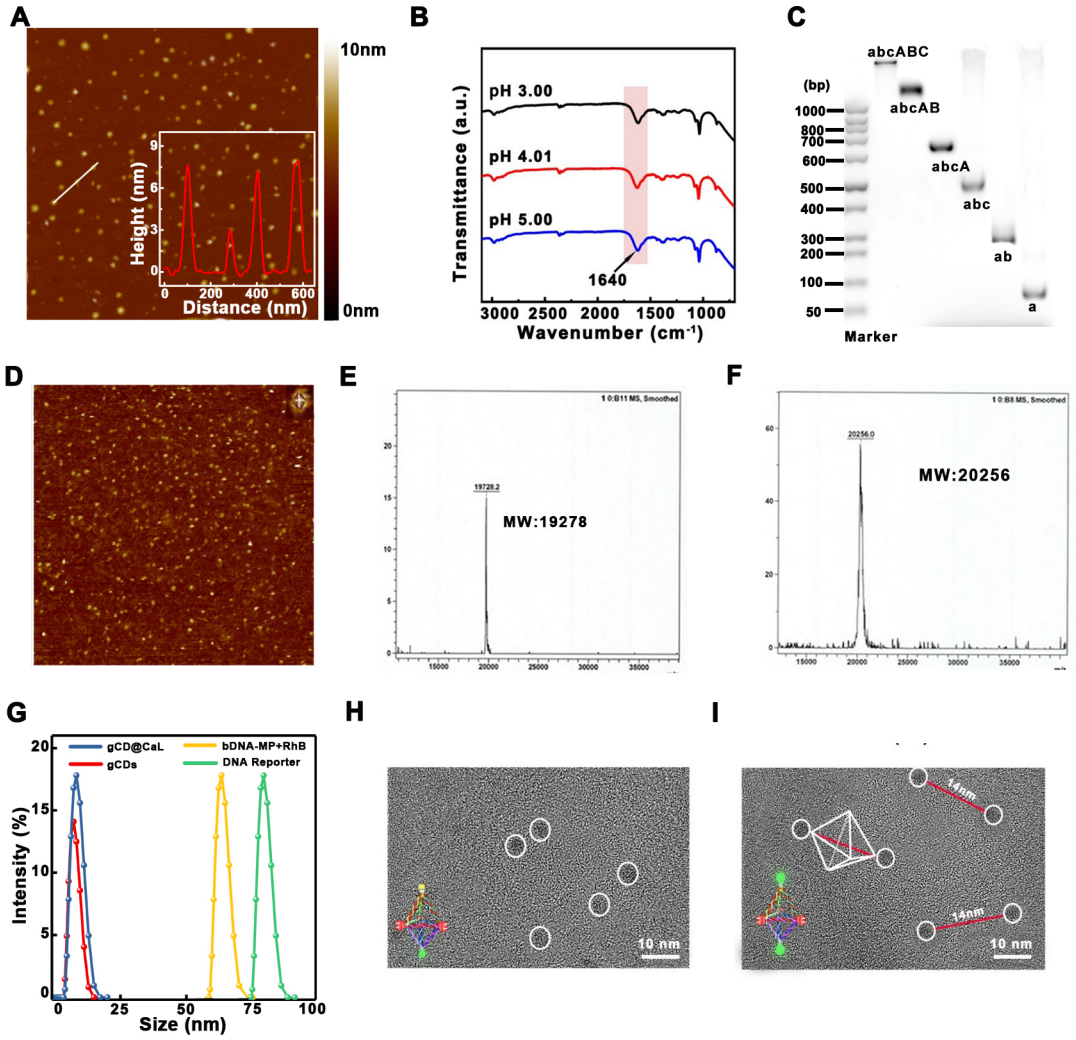

Figure S1. Characterization of gCDs, labeled-DNA and DNA Reporter. Related to Figure 1. (A) AFM image of gCDs. Insert shows the height distributions of gCDs along the line. (B) FT-IR spectra of gCD@CaL in different pH (3.00, 4.01, 5.00). (C) Native PAGE analysis of bDNA. From left to right are Marker, bDNA (abcABC), DNA-abcAB, DNA-abcA, DNA-abc, DNA-ab, DNA-a, respectively. (D) Bio-fast AFM image of bDNA. Inset shows overhead view of single bDNA. Scalebar = 1 μm. (E) Mass spectrum of MP-labeled DNA (a-MP). (F) Mass spectrum of RhB-labeled DNA (C-RhB). (G) Dynamic light scattering (DLS) data of gCDs, gCD@CaL, bDNA-MP+RhB and DNA Reporter. (H) TEM image of the developed DNA reporter (bDNA-MP+RhB+gCD@CaL). (I) TEM image of bDNA-1 assembled with two gCD@CaLs (bDNA-1-MP+gCD@CaL).

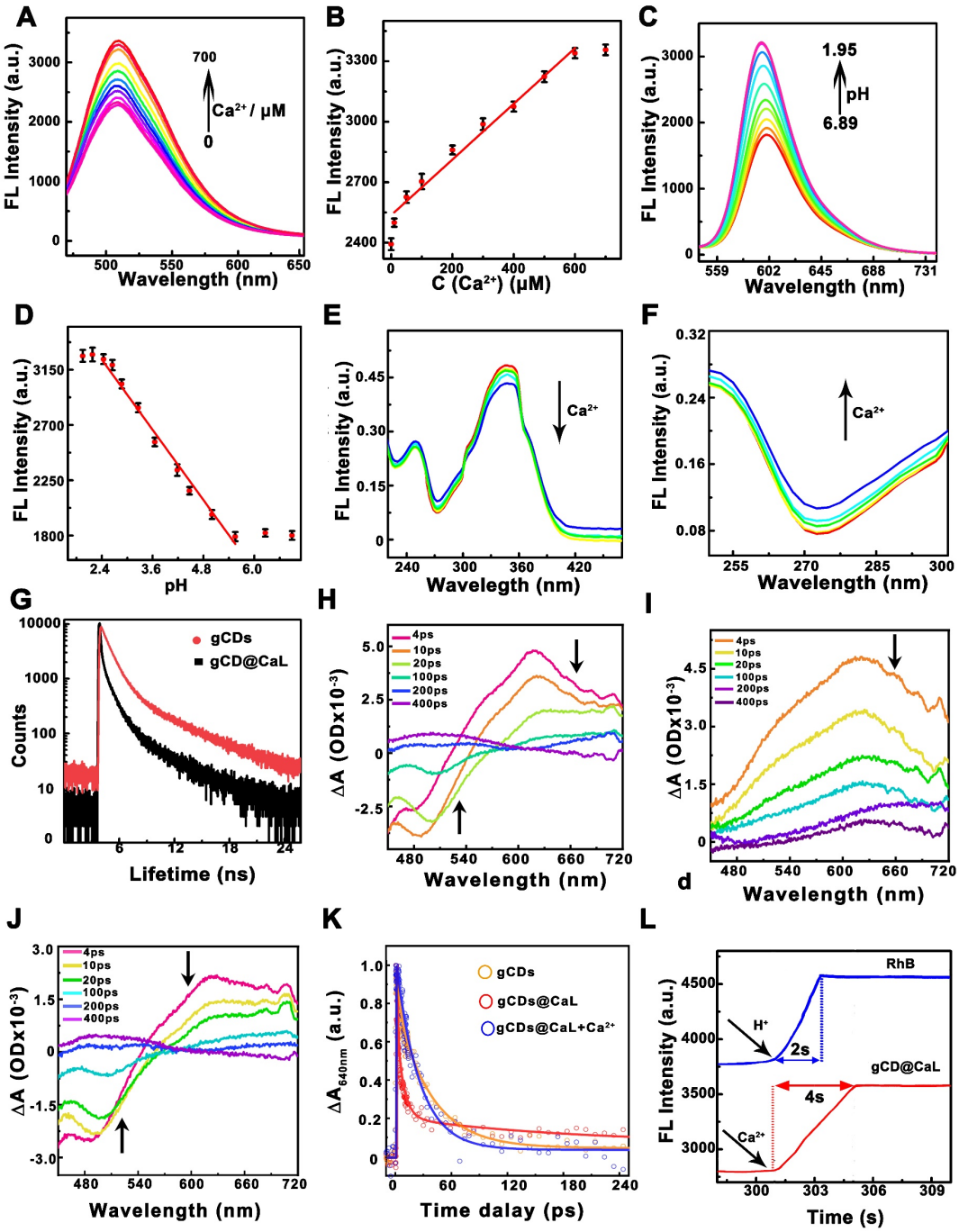

Figure S2. Fluorescence enhancement mechanism of gCD@CaL towards Ca^{2+}. Related to Figure 2. (A) Fluorescence itensity curves of gCD@CaL in the presence of different concentrations of Ca^{2+} (0, 1, 5, 10, 50, 100, 200, 300, 400, 500, 600 and 700 μM). (B) Calibration curve between fluorescence intensity (FL Intensity) and various concentrations of Ca^{2+} in (A). (C) Fluorescence intensity curves of pH probe with different pH values (1.95, 2.09, 3.29, 4.10, 5.02, 6.09, 6.58, 6.89). (D) Calibration curve between fluorescence intensity and various pH values in (C). (E) UV-vis absorption spectra of gCD@CaL in the presence of different

concentrations of Ca^{2+} (0, 100, 200, 300 and 400 μM). (F) Typical absorption spectra of gCD@CaL between 250-300 nm in the presence of different concentration of Ca^{2+} (0, 100, 200, 300 and 400 μM). (G) Fluorescence lifetime decay of gCDs and gCD@CaL. (H-J) TAS spectroscopic measurement for (H) gCDs, (I) gCD@CaL, and (J) gCD@CaL+Ca^{2+} after irradiation with a 640 nm laser flash. (K) Transient absorption kinetics of gCDs and gCD@CaL before and after addition of Ca^{2+} at an excitation wavelength of 640 nm. (L) Fluorescence response time of RhB and gCD@CaL.

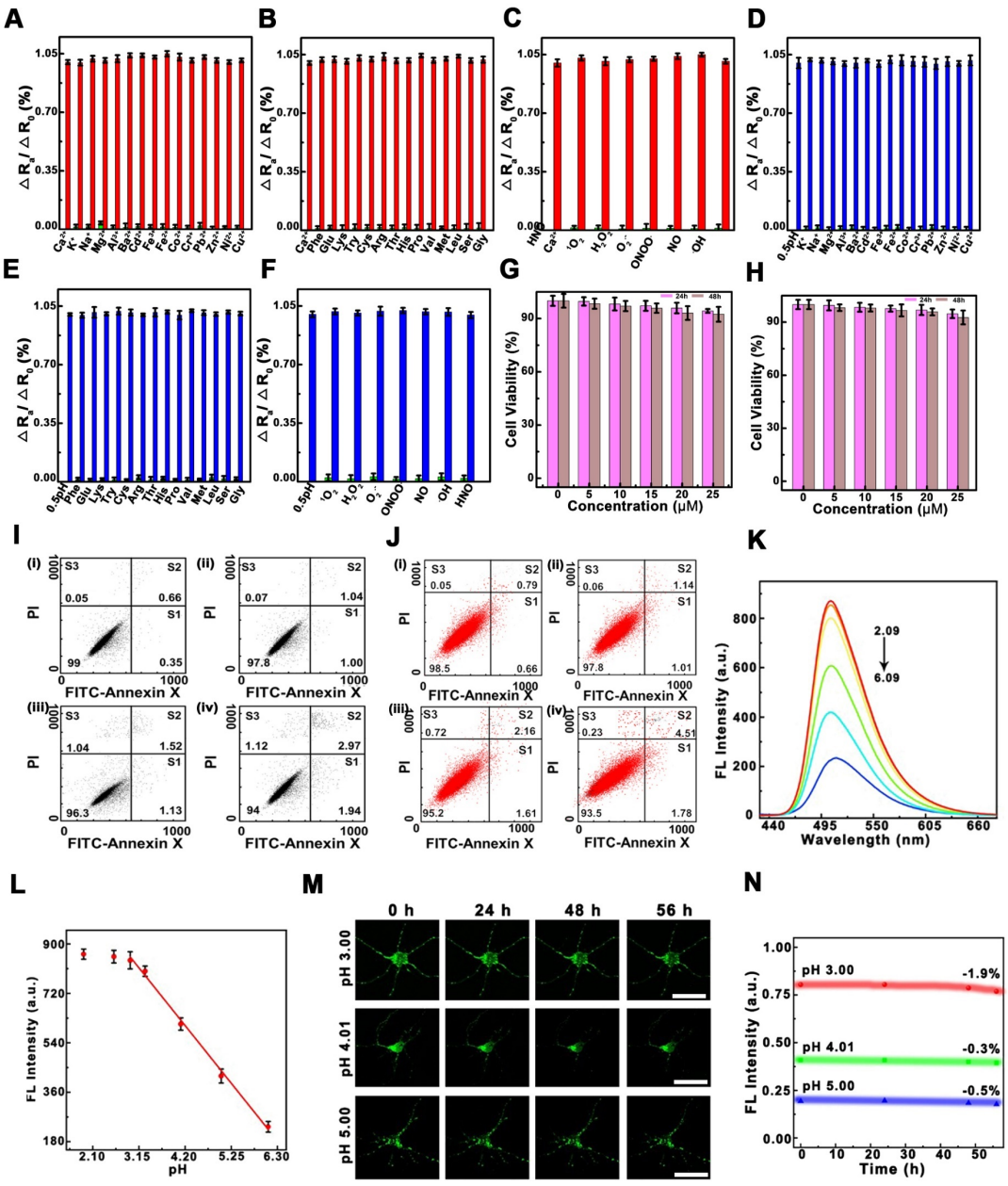

Figure S3. Selectivity, anti-interference investigation, cytotoxicity and biocompatibility of DNA Reporter. Related to Figure 3. Selectivity and competition tests of DNA Reporter towards various (A, D) metal ions, (B, E) amino acids and (C, F) common ROS, respectively. The green bars represent the influence of potential interferences to (A, B, C) gCD@CaL and (D, E, F) RhB channels on the DNA Reporter. The red bars represent the subsequent addition of Ca^{2+} to the nanoprobe solution with potential interferences. The blue bars represent the subsequent change of 0.5 pH with the existence of potential interferences. The concentration of metal ions (except K^+, Na^+ and Cu^{2+}): 300 μM. The concentrations of K^+, Na^+ and Cu^{2+}: 50 mM, 100 mM and 10 μM, respectively. (G) Viabilities of neurons after incubation for 24 h (pink

bars) or 48 h (brown bars) with different concentrations of nanoprobe at 37 ºC, respectively. (H) Viabilities of Neural stem cell after incubation for 24 h (pink bars) or 48 h (brown bars) with different concentrations of nanoprobe at 37 ºC, respectively. Cell apoptosis assay of neuron (I) and stem cell (J) after incubated with different concentrations: (a) 0, (b) 10, (c) 50, (d) 100 nM of nanoprobe for 24 h. (K) Fluorescence intensity curves of DND-189 obtained at different pH values (2.09, 2.58, 2.93, 3.29, 4.10, 5.02, 6.09). (L) Calibration curve between fluorescence intensity and pH value in (K). (M) The fluorescent imaging of gCD@CaL channel after DNA reporter entered in lysosomes for different times. (N) Time traces of gCD@CaL channel fluorescent intensity after DNA reporter entered in lysosomes for different times. Scale bar: 15 μm.

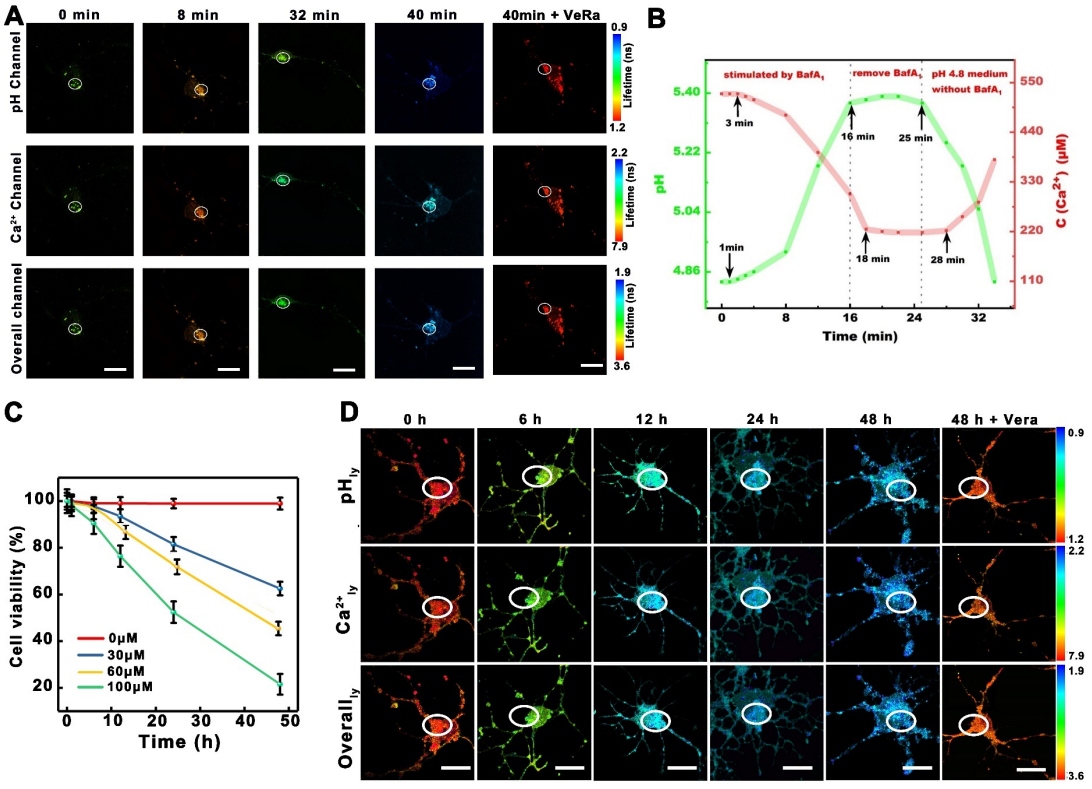

Figure S4. Fluorescence lifetime imaging of lysosomal Ca^{2+} and pH in neurons using the developed nanoprobe. Related to Figure 5, 6. (A) Fluorescence lifetime imaging and quantification of lysosomal pH and Ca^{2+} in neurons after the neurons were stimulated by bafilomycin A_1 for different times (0, 8, 32, 40 min and 40 min in the presence of VeRa). Scale

bar: 20 μm. (B) Time traces of different signals for lysosomal pH and Ca^{2+} with different stimulation. (C) Summarized data of neuron viability stimulated by aggregated $A\beta_{1-42}$ for different times (0, 6, 12, 24, and 48 h). (D) Confocal fluorescence lifetime images of neurons collected from pH, Ca^{2+}, and overall channels cultured with the developed nanoprobe in the presence of 25 μM aggregated $A\beta_{1-42}$ for different times. Scale bar: 15 μm.

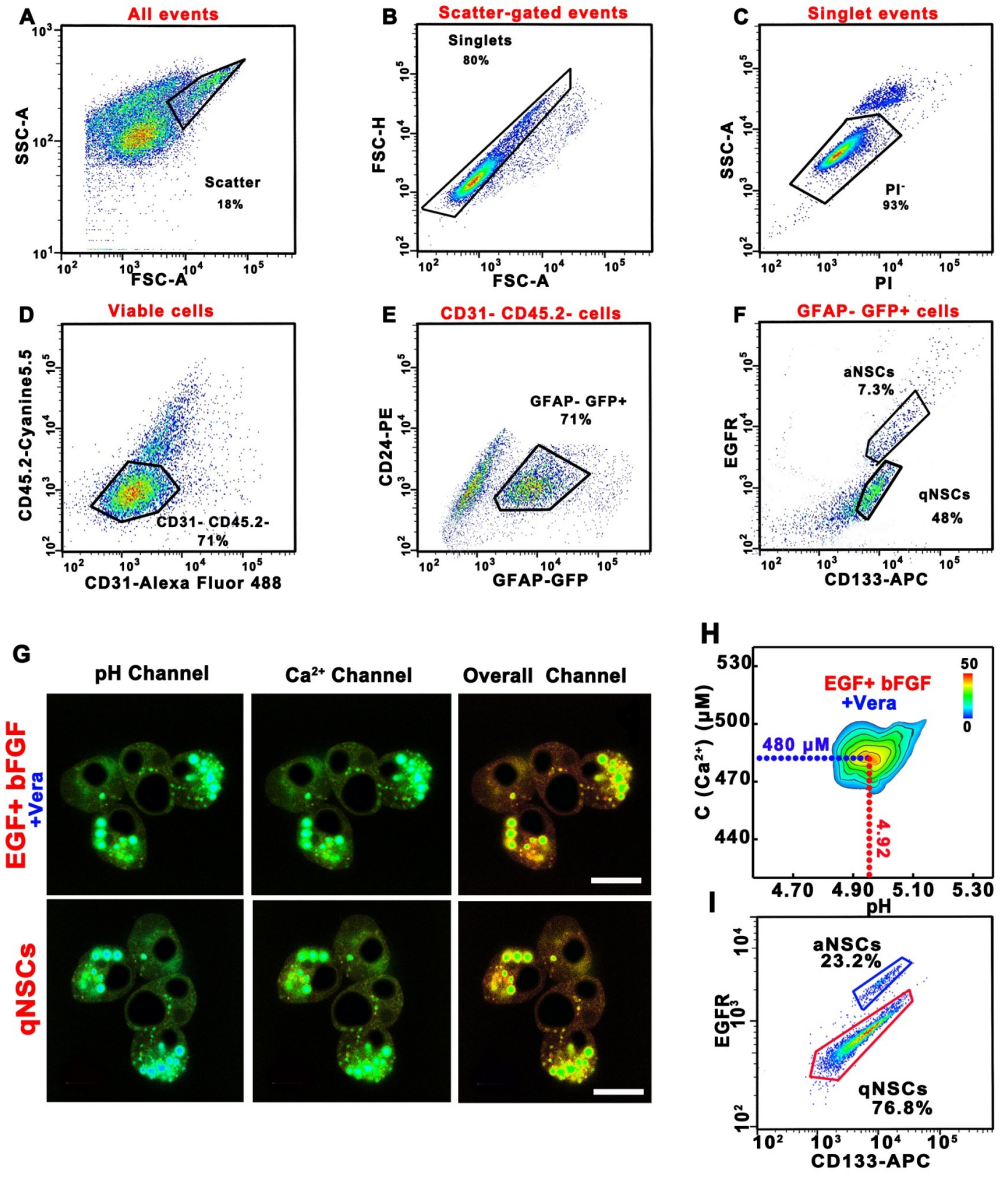

Figure S5. Isolation of stem cells and fluorescent lifetime imaging of lysosomal pH and Ca^{2+} in qNSCs. Related to Figure 7. (A-F) FACS sorting used to isolate qNSCs and aNSCs from the GFAP-GFP mice. (G) Confocal fluorescence lifetime images of qNSCs and qNSCs stimulated with EGF and bFGF in the presence of Vera collected from pH channel, Ca^{2+}

channel and overall channel. (H) Lysosomal density scatter profiles of qNSCs stimulated with EGF and bFGF in the presence of Vera. The density plot was pseudo color, here red and blue correspond to populations with higher and lower frequencies of occurrence. The data were obtained from 100 lysosomes in 10 cells. (I) FACS sorting used to isolate qNSCs and aNSCs after qNSCs stimulated with EGF and bFGF in the presence of Vera. Scale bar: 10 μm.

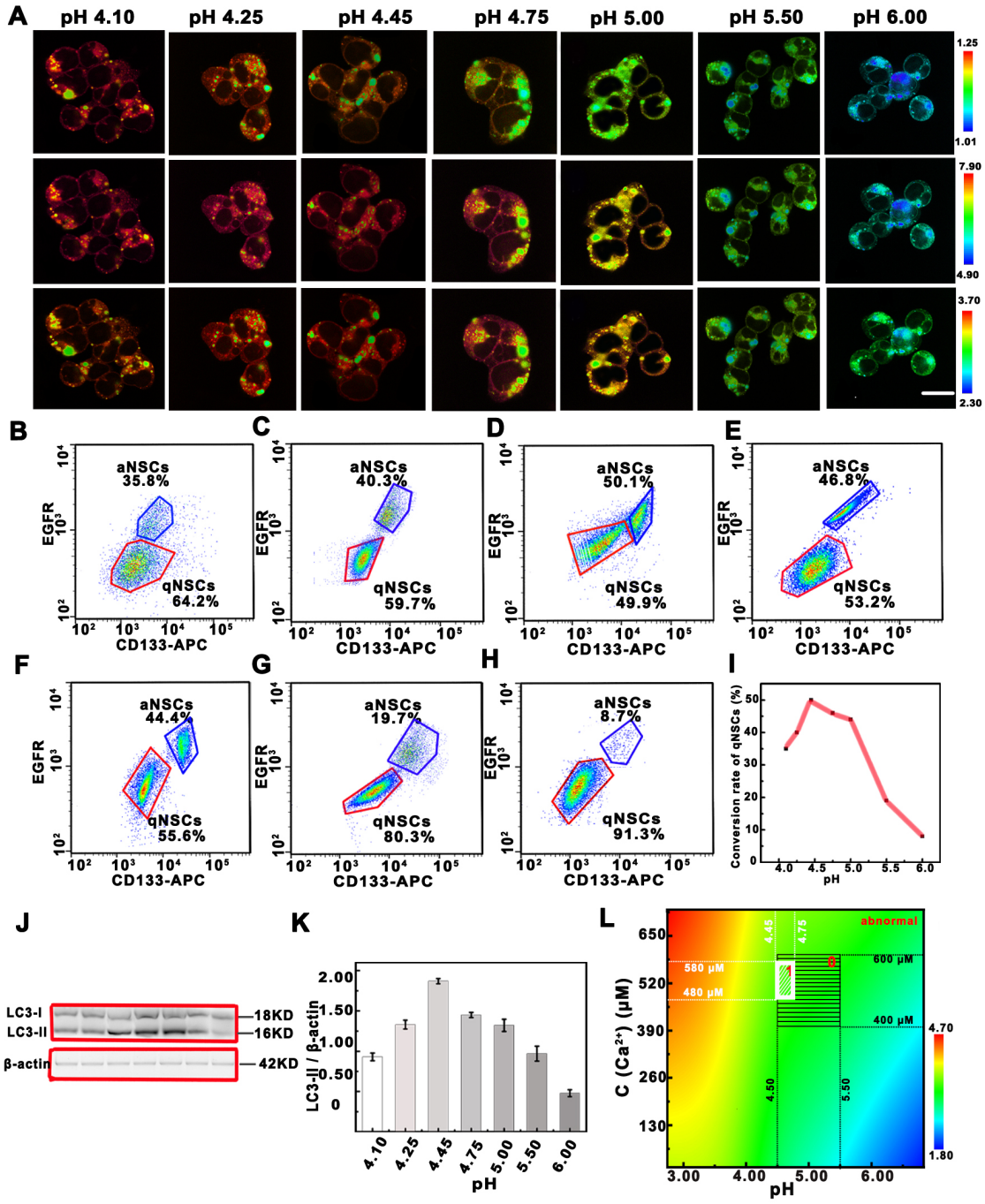

Figure S6. Imaging and simultaneous quantification of lysosomal Ca^{2+} and pH in qNSCs and aNSCs. Related to Figure 7. (A) Confocal fluorescence lifetime images of qNSCs collected from pH channel, Ca^{2+} channel and overall channel treated with nanoprobe at different pH (4.10, 4.25, 4.45, 4.75, 5.00, 5.50 and 6.00), respectively. (B-H) FACS sorting used to isolate qNSCs and aNSCs after qNSCs stimulated with (B) pH 4.10 (C) pH 4.25 (D) pH 4.45 (E) pH 4.75 (F) pH 5.00 (G) pH 5.50 (H) pH 6.00. **(I)** The transformation ratio of qNSCs in

different pH. (J) Immunoblotting analysis of relative levels of LC3-I, LC3-II in lysate. (K) The quantification of LC3-II / β-actin expression from western blot results. (L) Average fluorescence lifetime of the reporter at different pH values in the presence of different concentrations of Ca^{2+}. “Zone 1” represent “antiaging”, and “Zone 0” represent “aging”. Scale bar: 10 μm.

Data S1: Spectra of Products. Related to Scheme S1.

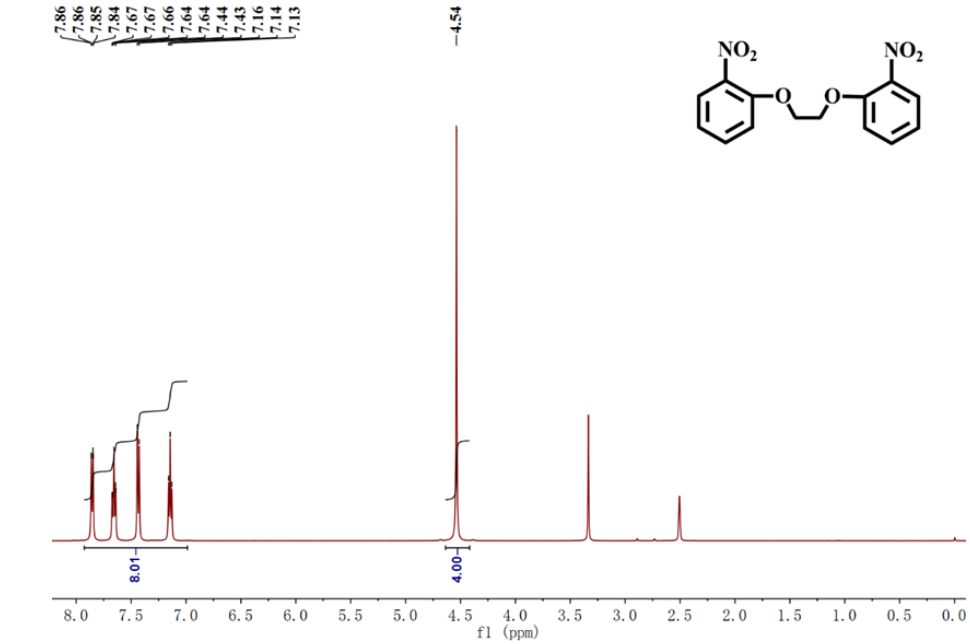

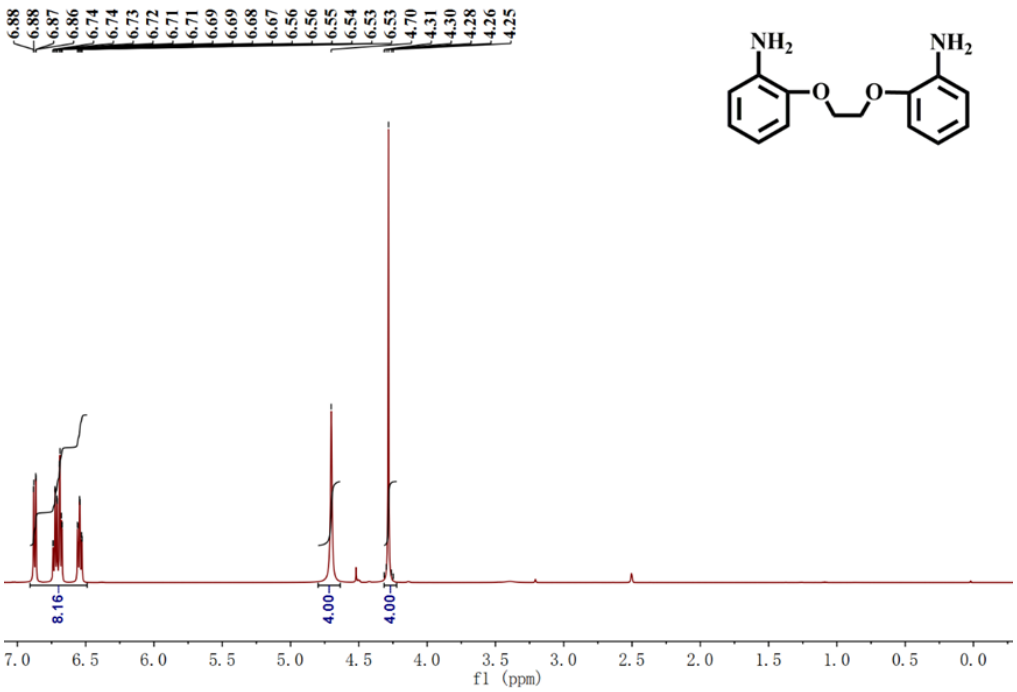

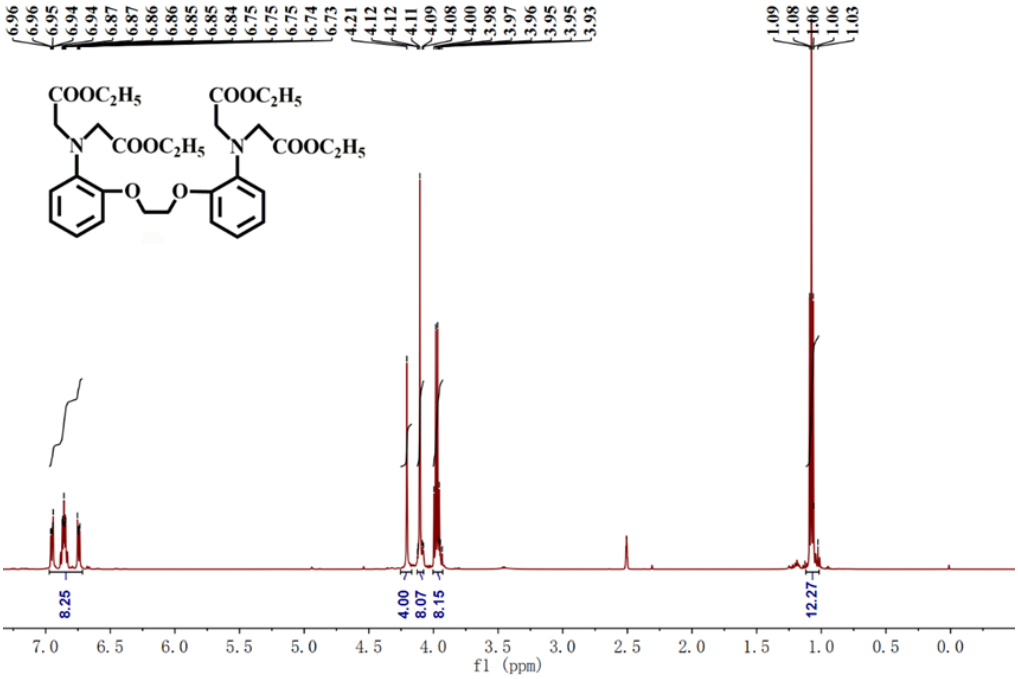
6.96 6.96 6.95 6.94 6.94 6.87 6.87 6.86 6.86 6.85 6.85 6.84 6.75 6.75 6.75 6.74 6.73
4.21 4.12 4.12 4.11 4.09 4.08 4.00 3.98 3.97 3.96 3.95 3.95 3.93
1.09 1.08 1.06 1.06 1.03
COOC2H5
N
COOC2H5
O
O
8.25
4.00
8.07
8.15
12.27
7.0 6.5 6.0 5.5 5.0 4.5 4.0 3.5 3.0 2.5 2.0 1.5 1.0 0.5 0.0
f1 (ppm)

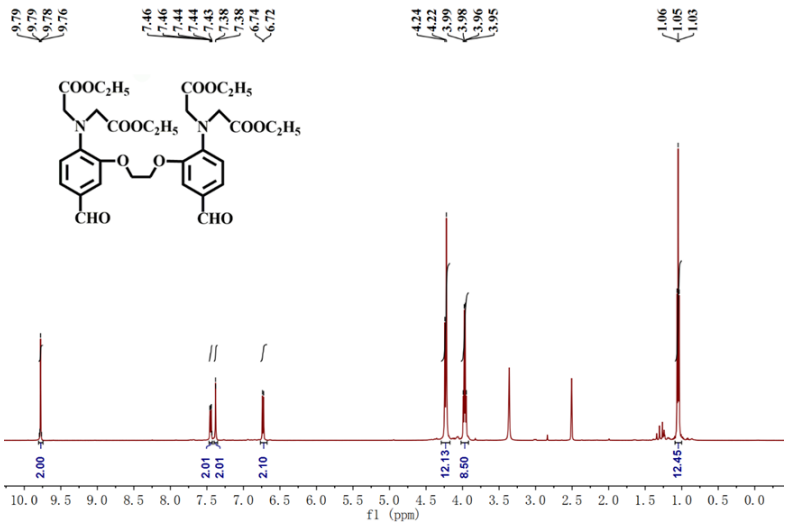
9.79 9.79 9.78 9.76
7.46 7.46 7.44 7.44 7.43 7.38 7.38 6.74 6.72
4.24 4.22 3.99 3.98 3.96 3.95
1.06 1.05 1.03
COOC2H5
N
COOC2H5
O
O
CHO
CHO
2.00
2.01
2.01
2.10
12.13
8.50
12.45
10.0 9.5 9.0 8.5 8.0 7.5 7.0 6.5 6.0 5.5 5.0 4.5 4.0 3.5 3.0 2.5 2.0 1.5 1.0 0.5 0.0
f1 (ppm)

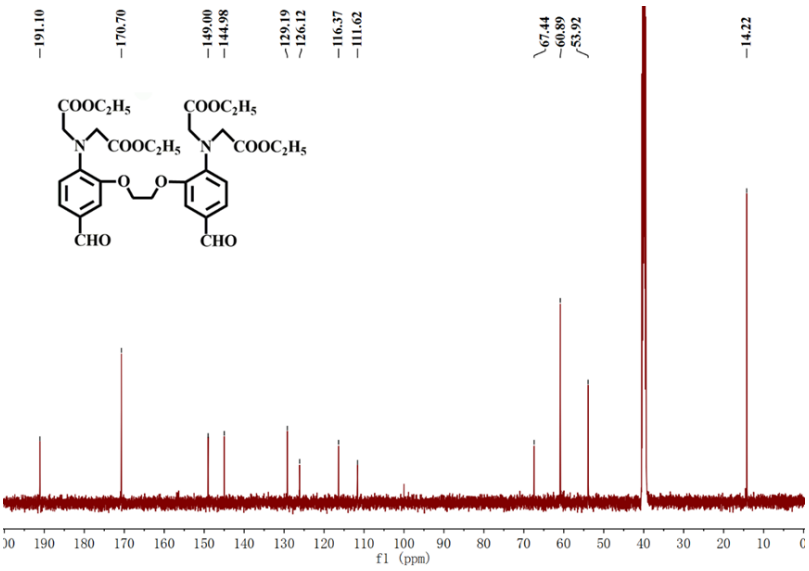

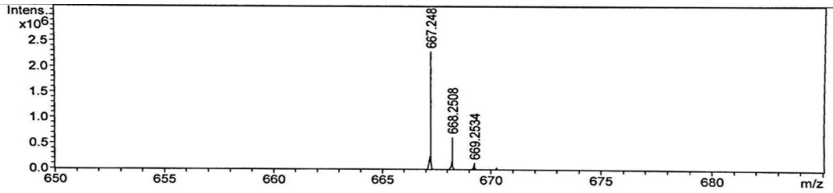

#	m/z	Res.	S/N	I	I %	FWHM
1	667.2482	42606	29090.1	2293944	100.0	0.0157
2	668.2508	33422	8066.2	635101	27.7	0.0200
3	669.2534	22237	1670.2	131235	5.7	0.0301
4	670.2567	17436	300.1	23536	1.0	0.0384

Meas. m/z	#	Ion Formula	m/z	err [ppm]	mSigma		Score	rdb	e⁻ Conf	N-Rule
667.2482	1	C32H40N2NaO12	667.2473	-1.3	45.7	9	38.93	13.5	even	ok

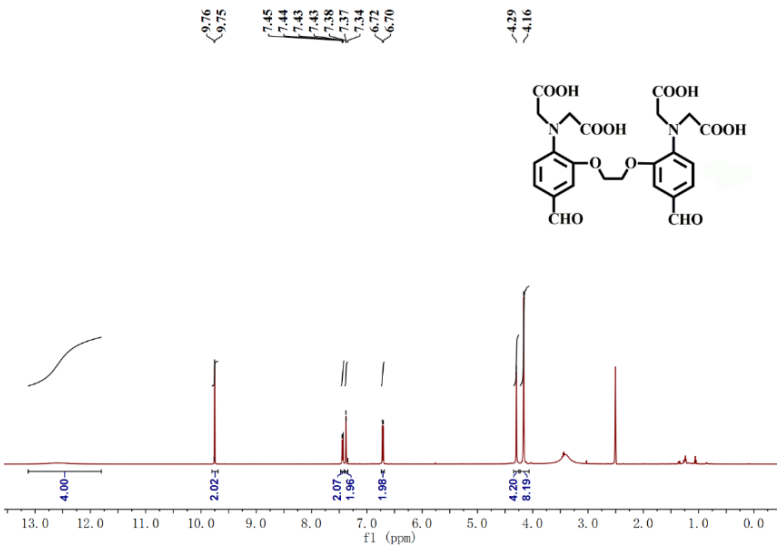

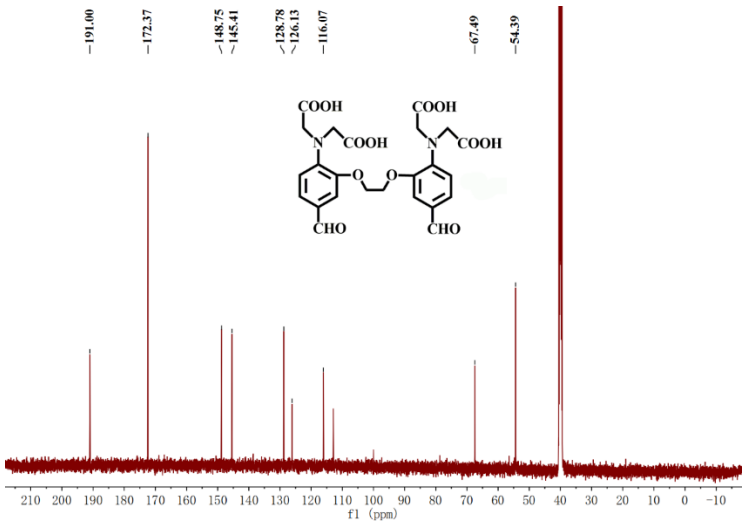

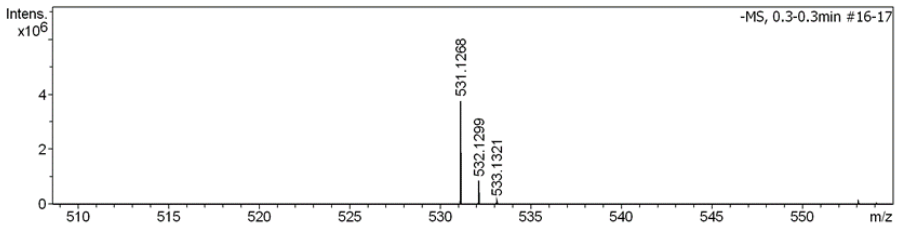

#	m/z	Res.	S/N	I	I %	FWHM
1	531.1268	44844	67768.2	3751421	100.0	0.0118
2	532.1299	45470	15194.1	840852	22.4	0.0117
3	533.1321	29960	2308.0	127736	3.4	0.0178

Meas. m/z	#	Ion Formula	m/z	err [ppm]	mSigma	mSigma	Score	rdb	e¯ Conf	N-Rule
531.1268	1	C24H23N2O12	531.1256	-2.2	28.5	28.5	79.92	14.5	even	ok

Transparent Methods

Chemical and Reagents. Sodium iodide, m-Nitrophenol, 1,2-dibromoethane, carbon powder (C), ethyl bromoacetate ($C_4H_7BrO_2$), dimethyl formamide (DMF), Iron(III) chloride hexahydrate, Potassium hydrogen phosphate anhydrous, 3-(4,5-dimethyl-2-thiazolyl)-2,5-diphenyl-2H-tetrazolium bromide (MTT) were purchased from Aladdin Chemistry Co. Ltd. (China). Hydrazine hydrate ($N_2H_4 \cdot H_2O$), dichloromethane (CH_2Cl_2), dimethyl sulfoxide (DMSO), methylbenzene, phosphorus oxychloride ($POCl_3$), ethyl acetate, acetonitrile, methanol (CH_3OH), ethyl alcohol (EtOH), sodium hydroxide (NaOH), potassium hydroxide (KOH), hydrochloric acid (HCl) and sodium bicarbonate ($NaHCO_3$), CuCl, KCl, NaCl, $CuCl_2$, $CaCl_2$, $FeCl_3 \cdot 6H_2O$, $MgCl_2 \cdot 6H_2O$, $ZnCl_2$, $AlCl_3$, $CdCl_2 \cdot 2.5H_2O$, $CrCl_3 \cdot 6H_2O$, $PbCl_2$, NaOAc, NaH_2PO_4 and $HgSO_4$ were obtained from Sinopharm Chemical Reagent Co. Ltd (China). Phosphate buffered saline (PBS), and 0.25% trypsin (with EDTA) were obtained from Hyclone Laboratories Company (U.S.A.). Penicillin (100 μg mL^{-1}) were purchased from Gibco Life Technologies Company (U.S.A.). Tryptophan (Trp), glutamine (Glu), lysine (Lys), histidine (His), cysteine (Cys), valine (Val), arginine (Arg), threonine (Thr), proline (Pro), leucine (Leu), methionine (Met), glycine (Gly), serine (Ser) were all obtained from Sigma-Aldrich (U.S.A.). All chemicals were analytical-grade and were used without further purification. All samples were prepared with ultrapure water purified by a Milli-Q water gradient system. DNA oligonucleotides modified with different groups were synthesized and purified by TaKaRa Biotechnology Co. Ltd (China) and listed in Table S1. For the selective text, Hydroxyl radical (•OH) was provided by the Fenton reaction of Fe^{2+} (10 μM) with H_2O_2 (60 μM). $^1O_2$ was produced from the reaction of H_2O_2 (10 μM) with NaClO (10 μM). Nitric oxide (NO) was obtained from the solution of SNAP. Peroxynitrite ($ONOO^-$) was generated by the reaction between $NaNO_2$ (10 μM) and H_2O_2 (10 μM). (ROO•) was derived from thermolysis of AAPH (10 μM) dissolved in air-saturated aqueous solution at 37 ºC.

Instruments. The nuclear magnetic resonance (NMR) spectra were collected on using a Bruker 500 MHz spectrometer (Bruker, Germany). Mass spectrum (MS) was obtained on using an Agilent 6890 spectrometer (Agilent, USA). UV−vis absorption spectrum was recorded on a UH5300 spectrophotometer (Hitachi, Japan). The gCDs were collected with a JEM-2100F transmission electron microscope (JEOL, Japan). Atomic force microscopic (AFM) images were recorded in the ScanAsyst mode under ambient conditions (Bruker, Germany). The fluorescence spectrum was obtained using a F-4600 fluorescence spectrophotometer (Hitachi, Japan). Fourier transform infrared spectroscopy (FTIR) spectra were collected on a Nicolet iS10 FTIR spectrometer (Thermo Fisher scientific, USA) at resolution of 4 cm^{-1} in the range 500−4000 cm^{-1}. Cell apoptosis assay experiments were

conducted by using a FACS Calibur flow cytometer (BD Biosciences, USA). Fluorescence confocal imaging were measured by Leica TCS-SP8 confocal laser scanning microscope (Leica, Germany). Fluorescence lifetime imaging was conducted on a TCS-SP8 confocal laser scanning microscope (Leica, Germany) equipped with a multiple-photon laser (PicoQuant, Germany) and TCSPC module SyPhotime-64 (Becker & Hickl, Germany).

Synthesis of Ca^{2+} ligand (CaL) CaL was synthesized according to the protocol reported in the literatures with modification, as shown in Scheme S1.

Compound b: NaOH (0.48 g, 1 mmol) and m-nitrophenol (1.53 g, 1 mmol) were dissolved in DMF (3 mL). The reaction mixture was stirred under 60 ºC for 20 min. And then, 1,2-dibromoethane (1 mL) was added and stirred at 130 ºC for 2 h. After the reaction, the mixture was cooled down to room temperature and diluted with water (100 mL). The formed yellow solid was collected by filtration, and washed with 10% (w/w) $NaHCO_3$ and water for at least three times. The products were purified by recrystallization from EtOH. Yield: 60%. (Figure S1) ^{1}H NMR (DMSO, 500 MHz), δ: 7.85 (d, 2H, J=8.1), 7.65 (t, 2H, J=8.0), 7.43 (d, 2H, J=8.5), 7.14 (t, 2H, J=7.8), 4.54 (s, 4H).

Compound c: A mixture of compound b (1.52 g, 5 mmol), carbon powder (0.075 g, 6 mmol), $FeCl_3$ (0.02 g, 0.01 mmol) and 90% (w / w) CH_3OH (15 g) were added into a dried three-necked flask equipped with a magnetic stirrer. When the mixture was heated to refluxing, 85% N_2H_4•H_2O (0.998 g) was added dropwise within 20 min. Then, the mixture was refluxed for 5 h. Without the mixture becoming cool, the carbon powder was removed by filtration and the reaction flask was rinsed with CH_3OH. The combined filtrate was evaporated and further purified by recrystallized from EtOH. Yield: 70%. (Figure S2) ^{1}H NMR (DMSO, 500 MHz), δ: 6.87 (dd, 2H, J=8.0), 6.71 (td, 2H, J=7.4), 6.66 (dd, 2H, J=7.8), 6.53 (td, 2H, J=7.6), 4.66 (s, 4H), 4.28 (s, 4H).

Compound d: Under nitrogen atmosphere, a mixture of compound c (1.54 g, 6 mmol), $C_4H_7BrO_2$ (4 ml, 36 mmol), NaI (0.38 g, 2 mmol) and K_2HPO_4 (7.212 g, 31 mmol) were stirred in 25 ml anhydrous acetonitrile and refluxed for 18 h. After the reaction, methylbenzene was added to the cooled mixture. The solution was washed with water and saturated brine. Organic layer was dried over Na_2SO_4, and then concentrated under vacuum and recrystallized from ethanol to give compound d. Yield: 62%. (Figure S3) ^{1}H NMR (DMSO, 500 MHz), δ: 6.99-6.91 (m, 2H), 6.86 (tt, 4H, J=7.4), 6.77-6.65 (m, 2H), 4.21 (s, 4H), 4.10 (s, 8H), 3.97 (m, 8H, J=7.1), 1.08 (t, 12H, J=7.2).

Compound e: A mixture of compound d (1.17 g, 2 mmol) and 150 μL pyridine was dissolved in 3 mL DMF. Then 1.2 mL $POCl_3$ was dropped slowly at 0 ºC. The reaction mixture was stirred at room temperature for 30 min and heated to 60 ºC for 1 h and then cooling down to room temperature for 20 h. The mixture was poured into aqueous NaOH mixed with ice. The aqueous layer was extracted with CH_2Cl_2 for three times or more. The combined organic layer was washed with water and saturated brine for several times. After

drying with Na_2SO_4 and evaporation, the residue was chromatographed on silica in petroleum ether: ethyl acetate = 4:1 (v / v) to yield 193 mg e. Yield: 20%. (Figure S4-6) ^{1}H NMR (DMSO, 500 MHz), δ: 9.78 (s, 2H), 7.45 (dd, 2H, J=8.3), 7.38 (d, 2H, J=1.8), 6.73 (d, 2H, J=8.3), 4.23 (d, 12H, J=10.4), 3.97 (q, 8H, J=7.1), 1.05 (t, 12H, J=7.1). 13C NMR (DMSO, 500 MHz): δ = 191.10, 170.70, 149.00, 144.98, 129.19, 126.12, 116.37, 111.62, 67.44, 60.89, 53.92, 14.22 ppm.

CaL: Compound **e** (130 mg, 0.2 mmol) was added into 3 mL KOH solution (1 M, dissolved in EtOH), then 1 mL CH_2Cl_2 was added. The mixture was stirred at 37 ºC for 24 h. After that, the mixture was adjusted to a pH range of 4 - 5 by HCl. The solid was filtered and product was extracted with abundant CH_2Cl_2. After drying with Na_2SO_4 and evaporation, 45 mg CaL ester was obtained. Yield: 40% (Figure S7-9). ^{1}H NMR (DMSO, 500 MHz), δ: 12.56 (s, 4H), 9.75 (s, 2H), 7.44 (dd, 2H, J=8.4), 7.38 (d, 2H, J=1.8), 6.71 (d, 2H, J=8.4), 4.30 (s, 4H), 4.16 (s, 8H). ^{13}C NMR (DMSO, 500 MHz): δ= 191.00, 172.37, 148.75, 145.41, 128.78, 126.13, 116.07, 112.88, 67.49, 54.39 ppm.

Preparation of Calcium probe. m-phenylenediamine (mPD) (0.1 g) was firstly dissolved in 90 mL ethanol, and then the solution was transferred into poly(tetrafluoroethylene)-lined autoclaves. After heating at 200 ºC in oven for 3 h and cooling down to room temperature naturally, gray suspensions were obtained from mPD. Then, the crude product was purified by dialysis bag (MWCO: 100-500 Da) in EtOH for at least 24 h. Finally, the purified gCDs were stored at 4 ºC for further use.

40 mg compound CaL-ester (**e**) (Scheme S1) was dissolved in 2 mL CH_2Cl_2. Then, gCDs were added to the solution, and stirred in water bath at 25 ºC for 6 h. And then, 2 mL EtOH of KOH (1 M) was add to the solution. Hydrolysis of gCD@CaL was stirred at 37 ºC for 6 h. Then, concentrated HCl was added to adjust its pH to about 5. Removed the CH_2Cl_2 by rotary evaporation. Compond **e** was conjugated onto gCDs through amino bond, and denoted as gCD@CaL.

Preparation of bipyramid DNA reporter for simultaneous determination of pH and Ca^{2+}. According to previous reports, different DNA sequences were designed and different molecular labeled DNAs (DNA-CHO, DNA-RhB and DNA-MP) were synthesized by Takara Bio (Erben et al., 2007). The reaction between the carboxyl group of RhB and the amino group of DNA was carried out to form the DNA-RhB. MP was coupled to DNA by a reaction between -NH_2 and -N=C=S of MP to form DNA-MP. First, DNA powder was centrifuged at 5000 rpm for 5 min, then carefully added different volumes of TM buffer (pH 8.0, 10 mM Tris-HCl, 300 mM NaCl, 5 mM $MgCl_2$) to the centrifuge tube containing DNA, dissolved the DNA overnight. Then the same concentration of DNA-RhB, DNA-MP, DNA-MP, DNA-MP, DNA-CHO and DNA-b were mixed and heated to 95 ºC for 5 min, rapidly cooled to 4 ºC and kept at 4 ºC for at least 30 min, a bDNA-MP + RhB probe was formed. Subsequently,

100 μL of bDNA-MP + RhB probe (10 μM) was added to 10 μL of gCD@CaL (4.9 mg / ml) and reacted at room temperature for at least 6 h to form DNA Reporter (bDNA-MP + RhB + gCD@CaL). Then, the produced nanoprobe was purified by 0.22 μm Millipore ultrafiltration, and the obtained DNA Reporter was stored at 4 ºC for use.

Primary culture of mouse cortical neurons and neural stem cells. The animal experimental protocols were approved by Animal Care and Use Committee of East China Normal University, Shanghai, China. Primary cultures of mouse cortical neurons and stem cells were prepared as reported previously. Briefly, postnatal one day *C57BL/6 WT* and *GFAP-GFP C57BL/6* mice were anesthetized with halothane for extracting neurons and stem cells respectively. Brains were removed rapidly and placed in ice-cold Ca^{2+} and Mg^{2+} free phosphate-buffered saline (PBS). Tissues were dissected and incubated with papain for 15 min at 37 ºC, followed by trituration with fire-polished glass pipettes, and plated in poly-D-lysine-coated 33-mm Petri dishes with 20 mm bottom wells at a density of 1×10^6 cells per dish. Neurons were cultured with Neurobasal medium supplemented with B27 and L-Glutamine, and stem cells were contained with DMEM/F12 medium with B-27, N-2 supplement and glucose. Then cells were maintained at 37 ºC in a humidified atmosphere containing 5% CO_2. Cultures were fed twice a week and used for all the assays 7-10 days after plating.

FACS sorting of qNSCs and aNSCs. NSCs were separated from *GAFP-GFP* mice and used for FACS analysis following the previously protocol. The isolated stem cells were digested for 5 min at 37 ºC with papain, centrifuged, and the cells were re-dispersed in a centrifuge tube with ice-cold Ca^{2+} and Mg^{2+} free phosphate-buffered saline (PBS). Then, the suspended cells were stained with Alexa Fluor 488 anti-mouse CD31 (Biolegend, 102414), PerCP/Cyanine5.5 anti-mouse CD45.2 (Biolegend, 109828), PE anti-mouse CD24 (Biolegend, 101808), APC anti-mouse CD133 (Biolegend 141208), EGFR (Invitrogen, MA5-13070) respectively. The cells were then washed and stained with streptavidin PEcy7 (Invitrogen, SA1012). Adding Propidium iodide (PI) for live cells identification, and then the cells were used for Fluorescence Activating Cell sorting (FACS). All the steps were performed on ice after the papain digestion.

Cytotoxicity and Apoptosis Assay. For cytotoxicity assays, different concentrations of DNA Reporter (0, 5, 10, 15, 20 and 25 μM) and $A\beta_{1\text{-}42}$ (0, 30, 60 and 100 μM) were added to 96 wells plates. The plates were preincubated with neurons or stem cells for 48 hours. Subsequently, 20 uL of 3-(4,5-dimethyl-2-thiazolyl)-2,5-diphenyl-2H-tetrazole bromide (MTT) was added to each well. After reacting for 4 hours, the mixed solution was removed, and 80 μL of DMSO was added. Then, the absorbance was measured at 490 nm after shaking cells for 5 min. Cell viability was determined according to the following formula:

cell viability (%) = the absorbance of experimental group/the absorbance of blank control group × 100%. For apoptosis assay, different concentration of DNA Reporter (0, 10, 50, 100 nM) were cultured with neurons and stem cells for 24 h. Then the cells were digested and re-suspended in 300 μL of binding buffer and further stained by FITC−annexin V and PI to label the apoptosis cells and necrotic cells, respectively, for FACS measurement.

Fluorescence confocal lifetime Imaging. The medium containing the nanoprobes (50 nM) was added to the cells and incubated for 30 min. The adherent cells were then washed three times with HBSS to remove nanoprobes that were not absorbed by the cells. Then, the cells were cultured in a mixture solution of neurobasal medium and Britton-Robinson (BR) buffer (40 mM) contains 120 mM KCl, 30 mM NaCl, 1 mM NaH_2PO_4 and 5 mM glucose at different pH values (4.00, 4.90, 6.09, 6.70) for 30 min in the presence of 10 μM nigericin (H^+/K^+ ionophore). After that, the cells were washed twice with HBSS and subjected to confocal fluorescence lifetime imaging. Excitation was performed using a 405 nm diode laser. Fluorescence lifetimes were collected from gCD@CaL (450-550 nm) and RhB (610-700 nm), respectively. Ca^{2+} imaging in cells was similar to pH imaging after the neurons were stimulated by 25 μM EGTA in the presence of calcimycin (a divalent cation ionophore) to chelate Ca^{2+} to validate Ca^{2+}-induced fluorescence lifetime changes. For neurons stimulated by bafilomycin A_1, 10 μM bafilomycin A_1 incubated the cells for different time (0, 20, 40, 60 min), then the cells were washed twice with HBSS for three times. After that, the cells were incubated with 50 nM nanoprobe for 15 min and subjected to fluorescence lifetime imaging. To inhibit the changes of the concentration of lysosomal Ca^{2+}, the cells were stimulated by 10 μM bafilomycin A_1 in the presence of 10 μM Ca^{2+} channel inhibitor verapamil (VeRa). For Aβ stimulated cells, neurons were first incubated in medium containing 60 μM Aβ for different times (0, 6, 12, 24,48 h) and then washed three times with HBSS. Next, 50 nM nanoprobes were added and incubated for 30 min. Fluorescence lifetime imaging was performed after washing neurons three times with HBSS.

Immunochemical analyses. For lysosomal pH and Ca^{2+}- regulated autophagy, after the cells were treated with different pH and stimulated by bafilomycin A_1 for different times, the cells were lysed and extracted to sodium dodecyl sulfate polyacrylamide gel electrophoresis (PAGE) and transferred to a nitrocellulose filter (NC) membrane. The NC membrane was then blocked with 5% skim milk for 1 h at room temperature. Next, the membrane was further incubated with the primary antibody LC3B Polyclonal Antibody (Sigma L7543) overnight at 4 °C. After washing 3 times with PBS (containing 0.5% Tween-20, pH 7.5), it was incubated with horseradish peroxidase-labeled secondary antibody (EASEN, 18630) for 1 h at room temperature. The signal detection was performed with chemiluminescence. All Western blots shown were repeated at least five times with similar results.